UNIVERSITY OF BIRMINGHAM
University of Birmingham Research at Birmingham

In situ alloying based laser powder bed fusion processing of β Ti–Mo alloy to fabricate functionally graded composites

Duan, Ranxi; Li, Sheng; Cai, Biao; Tao, Zhi; Zhu, Weiwei; Ren, Fuzeng; Attallah, Moataz M.

DOI:
10.1016/j.compositesb.2021.109059

License:
Creative Commons: Attribution-NonCommercial-NoDerivs (CC BY-NC-ND)

Document Version
Peer reviewed version

Citation for published version (Harvard):
Duan, R, Li, S, Cai, B, Tao, Z, Zhu, W, Ren, F & Attallah, MM 2021, 'In situ alloying based laser powder bed fusion processing of β Ti–Mo alloy to fabricate functionally graded composites', *Composites Part B: Engineering*, vol. 222, 109059. https://doi.org/10.1016/j.compositesb.2021.109059

Link to publication on Research at Birmingham portal

General rights
Unless a licence is specified above, all rights (including copyright and moral rights) in this document are retained by the authors and/or the copyright holders. The express permission of the copyright holder must be obtained for any use of this material other than for purposes permitted by law.

•Users may freely distribute the URL that is used to identify this publication.
•Users may download and/or print one copy of the publication from the University of Birmingham research portal for the purpose of private study or non-commercial research.
•User may use extracts from the document in line with the concept of 'fair dealing' under the Copyright, Designs and Patents Act 1988 (?)
•Users may not further distribute the material nor use it for the purposes of commercial gain.

Where a licence is displayed above, please note the terms and conditions of the licence govern your use of this document.

When citing, please reference the published version.

Take down policy
While the University of Birmingham exercises care and attention in making items available there are rare occasions when an item has been uploaded in error or has been deemed to be commercially or otherwise sensitive.

If you believe that this is the case for this document, please contact UBIRA@lists.bham.ac.uk providing details and we will remove access to the work immediately and investigate.

Download date: 03. May. 2024

In situ Alloying Based Laser Powder Bed Fusion Processing of β Ti-Mo Alloy to Fabricate Functionally Graded Composites

Ranxi Duan[a, b], Sheng Li[b], Biao Cai[b,*], Zhi Tao[a], Weiwei Zhu[a], Fuzeng Ren[a,*], Moataz M. Attallah[b,*]

[a] *Department of Materials Science and Engineering, Southern University of Science and Technology, Shenzhen, Guangdong, 518055, China.*

[b] *School of Metallurgy and Materials, University of Birmingham, B15 2TT, United Kingdom*

Corresponding Author. E-mail: renfz@sustech.edu.cn (F. Ren); B.Cai@bham.ac.uk (B. Cai); and M.M.Attallah@bham.ac.uk (M. M. Attallah)

Abstract

β-titanium (Ti) alloys combined with high strength and good ductility have attracted extensive research interest for use in many advanced industrial applications. In this study, laser powder bed fusion (LPBF) parameters were firstly optimised to fabricate highly dense metastable β Ti-12Mo alloy with largely homogeneous structure from low-cost elemental powders. When the laser area energy density (AED) increased to 4 J/mm^2 under the simple scan mode, the refractory Mo powder melted and dissolved into the Ti matrix due to the increased melting pool temperature and increased cycles of remelting. However, when the same high AED was used in the chess scanning mode, keyhole-induced defects emerged at the island boundaries. The laser beam delay (LBD) and island spacing (IS) settings were optimised to eliminate keyhole defects. Additionally, it is found that using low and high AED (e.g. 1.6 and 4 J/mm^2), the builds show significantly different microstructure and mechanical properties. In view of this, a Ti-Mo functional gradient composite (FGC) was fabricated via alternating AEDs of 1.6 and 4 J/mm^2 layer-wise. A gradient distribution of α" phase with varied size and quantities across the designed layer boundaries was produced. The Ti-Mo FGCs possessed a high compressive yield strength of 1173 (± 15) MPa and improved strain hardening capacity. The developed approach demonstrated the potential for the fabrication of FGCs using an in situ alloying based LPBF.

***Keywords**:* Laser powder bed fusion; In situ alloying; β-titanium alloys; Functional gradient composite; Layered structures

1. Introduction

Metastable β-Titanium (Ti) alloys have a wide range of potential structural and biomedical applications due to their high specific strength, low modulus, and excellent fatigue and corrosion resistance [1, 2]. Ti-Mo alloys are among the most promising metastable β-Ti alloys, which exhibit high ultimate strength and exceptional ductility [1, 3]. However, Ti-Mo based alloys are difficult to be fabricated using conventional methods, such as vacuum arc melting and powder metallurgy. Due to the high melting point of Mo and the low interdiffusion rate between Mo and Ti [4], vacuum arc melting of Ti-Mo alloys usually requires several remelting cycles, followed by long-term homogenisation heat treatment [5, 6]. For the powder metallurgy route, preparing pre-alloyed powders through atomisation is expensive and time-consuming [7]. In addition, machining β-Ti alloys is not easy because of their low thermal conductivity, which reduces the heat diffusion between the tool and workpiece and decreases the tool life [8, 9]. Therefore, it is of interest to find an alternative low-cost approach to fabricate β Ti-Mo alloys in a near-net-shape form.

Recently, laser powder bed fusion (LPBF), a disruptive additive manufacturing (AM) technology, has demonstrated significant potential for the fabrication of β-Ti alloys [10]. Several β-Ti alloys have been successfully fabricated using LPBF [10, 11], such as Ti-24Nb-4Zr-8Sn (weight percent, and hereafter) [10], and Ti-15Mo-5Zr-3Al [11]. However, most previous studies used pre-alloyed powders, which require long processing cycles, including preparing homogeneous ingots and atomisation processes, which is expensive due to the low powder yield in the optimum size range (approximately 15–60 μm) for LPBF [7]. In situ alloying of the blended powders is, therefore, attractive for the AM fabrication of β-Ti alloys, which has been demonstrated in Ti alloys [12-14], steels[15], Ni-based superalloys[16],NiTi alloys[17], and Zn alloys[18]. Using in situ alloying methods, instead of pre-alloyed powders,

to process Ti alloys, is cost-effective and offers great opportunities to produce non-conventional alloys [19-22]. However, unmelted refractory elemental particles and inhomogeneous element distribution have been observed in the β-Ti alloys fabricated using in situ alloying methods [13] due to the high melting points and low interdiffusion rates of the refractory alloying elements in Ti-based alloys [4]. For instance, Mo has a melting point of 2,623°C, which is approximately 1,000°C higher than that of Ti (1,668°C). The laser reflectance of Mo is also higher than Ti [23]. These factors mean that it is hard to melt the Mo particles completely. Although the elements are completely soluble [13], according to the Ti-Mo phase diagram, previous studies have shown extremely low interdiffusion coefficient between Ti and Mo in the range from 10^{-14} to 10^{-11} m^2/s depending on the homogenisation temperatures [4]. Therefore, it is challenging to produce Ti-Mo alloys without unmelted Mo particles that are free from chemical heterogeneity using in situ alloying based LPBF. In our previous work, the microstructure and mechanical properties of the Ti-12Mo-6Zr-2Fe alloy fabricated by LPBF in situ alloying have been presented [2]. In this study, the optimisation and processing conditions (mainly the input laser power density) for LPBF of a Ti-Mo binary alloy are presented, which would allow the dissolution and homogenisation of Mo in Ti matrix.

Keyhole-induced defects form during LPBF, which lead to low fatigue strength and premature failure [24]. Therefore, the reduction of keyhole defects is essential for the structural integrity of the printed components. When the energy input increases, the melt pool transfers from a shallow and semicircular shape to a narrow and deep shape, forming the keyhole [24]. Although the keyhole might facilitate the absorption of laser and energy efficiency relatively, it could be trapped in the components due to the defects caused by the laser's multiple reflections inside the keyhole [25]. Recently, the high-speed synchrotron X-ray radiographic observations [24] revealed that keyholes formation followed the sequence of vaporisation, suppression of the liquid surface, instability, and then pore formation. The suppression of the liquid surface was caused by the recoil pressure [26], which formed as a result of vaporisation [27]. The acoustic waves generated by the keyhole instability are also a key driving force for

its formation [28]. In this work, when the optimised laser processing parameters to melt and homogenise Mo in the Ti-Mo alloy were identified, keyhole defects were introduced. Then, the laser scanning parameters were optimised further, which largely eliminated the keyhole defects.

Nature creates functional gradient structure to obtain a biological system with high strength and toughness to endure the complex natural environment [22, 29]. These bioinspired gradient systems have proved their superiority to the conventional homogeneous structure [30]. Several methods have been developed to manufacture bioinspired gradient metallic structure, such as the surface mechanical attrition treatment [31], and high-pressure torsion [32]. The gradient structure shows an excellent combination of high strength and ductility. Recently, laser additive manufacturing has been used to process gradient structure. Different laser scanning parameters could introduce significantly different thermal history during processing [33], which means that it could be a potential method to produce the bioinspired gradient structure by varying the processing parameters. Philipp *et al*. [34] have produced a Damascus steel with a microstructure of alternating soft and hard layers by controlling the laser scanning pauses,which illustrated improved mechanical properties than ancient Damascus steel. In this work, we explored the feasibility of using an in situ alloying based LPBF to produce FGCs.

In this study, a processing route for the fabrication of Ti-Mo alloys and Ti-Mo FGC using an in situ alloying based LPBF is presented. The contribution of this study is two-fold: (1) LPBF in situ alloying is demonstrated to be a promising manufacturing route for new alloy fabrication when pre-alloyed powders are challenging to produce; and (2) in situ alloying LPBF could be used to create components with gradient composition and microstructure, which has the potential to fabricate high-performance FGCs.

2. Experimental

2.1 Powders

Gas atomised pure Ti (Purity>99.9%) and Mo (Purity>99.9%) powders (TLS Technik GmbH, Germany) were used as the base powders for Ti-12Mo powder blends. Both Ti and Mo

powders were spherical. The Ti powder had a size in the range of 20-63 μm, and a d50 of 42.9 μm (Fig. 1a), while the Mo powder was sieved using 50 μm sieves and had a particle size in the range of 5-45 μm and a d50 of 20.7 μm (Fig. 1a). The mixed powders were blended for 24 h using a tumbler mixer (Fig. 1b), under the protection of an Argon atmosphere. As shown in the backscattered electron (BSE) micrograph (Fig. 1c), no agglomeration of the Mo powders in the blended powders was observed, suggesting a uniform blending.

The flowability of the pure Ti powder and Ti-12Mo mixed powders were tested using the RST-XS Schulze Ring Shear Tester (Germany), in accordance with the standard of ASTM-D6773 [35], to ensure appropriate spreading during LPBF (Table 1). The flow function coefficient (F.F.C), which indicates the powder flowability, was >10 in the blended powders, indicating free-flowing powders. In addition, the Hausner ratio was measured, and there was good flowability because the Hausner ratio was <1.25. This shows that the flowability of blended powders of Ti and Mo is as good as that of pure Ti powders.

2.2 LPBF Process

All specimens and components were fabricated using a Concept Laser M2 Cusing® LPBF system, which was equipped with a 400 W Nd:YAG continuous laser source and a laser spot diameter of ~70 μm. The LPBF in situ alloying processing is shown in Fig. 1d. The Ti6Al4V plate, with a dimension of 90 mm × 90 mm, was used as the substrate for the fabrication. The builds were carried out using a 20 μm powder layer thickness under a controlled argon atmosphere, where the oxygen content was ~1000 ppm. The oxygen and nitrogen content of the fabricated Ti-12Mo samples were measured using the ON736 elemental analyser (LECO, US), which was 0.236 (± 0.010) wt% and 0.091 (± 0.008) wt%, respectively. Simple scan and chess (island) scan strategies (Fig. 1e) were used with varied input energy, scanning speed, and hatch spacing, as shown in Table 2. The island spacing (IS; the overlap of neighbouring islands) and the laser beam delay (LBD; laser dwelling time) were optimised to obtain samples without

defects (Fig. 1f). To represent an equivalent heat input in LPBF, when different processing parameters were applied, the laser area energy density (AED) was calculated [36], which is given by:

$$AED(J/mm^2) = \frac{Laser\ Power(W)}{Scan\ speed(mm/s) \cdot Hatch\ spacing(mm)} \quad (1)$$

2.3 Microstructural Characterisation

The fabricated specimens were sectioned for microstructural characterisation and mechanical testing using electrical discharge machining. For scanning electron microscopy (SEM) and optical microscopy (OM) observations, the specimens were sequentially ground with 220- and 1200-grit papers, polished using MD-Chem with OPS-H_2O_2 solution (Struers, Denmark), and etched using Kroll's reagent (2% HF + 6% HNO_3 + 92% distilled water) for 30 s. Zeiss Axioskop 2 microscopes were used for OM observation. The microstructure of the polished samples was studied using SEM (TESCAN MIRA 3, Czech Republic) operated in secondary electron and BSE imaging modes (without etching). The elemental distribution was analysed using energy dispersed X-ray spectroscopy (EDS) performed using X-Max^N Silicon Drift EDX Detector (Oxford Instruments, Oxford, UK), equipped in SEM, and electron probe microanalysis (EPMA) characterised by a JXA-8530 analyser (JEOL, Tokyo, Japan). The crystallographic orientation and local misorientations were characterised using electron backscattering diffraction (EBSD) with a step size of 0.5 μm and analysed using Channel 5 software. In addition, the microstructure was investigated using a transmission electron microscope (TEM; Tecnai F30, FEI, US) operated at 300 kV. The high-angle annular dark-field scanning TEM (HAADF-STEM) imaging and EDS mapping were performed on an FEI Talos TEM at 200 kV. The TEM samples were prepared using focus ion beam (FIB; Dual Beam Heilos^{TM} Nanolab 600i, FEI) milling. X-ray diffraction (XRD) patterns were recorded using a Rigaku Smartlab-9kW diffractometer (Rigaku, Tokyo, Japan) in the 2θ range of 20˚-100˚ with Cu-Kα radiation (λ = 1.54056 Å, 45 kV, 200 mA). The specimens' densities were measured by a Practum 224 balance (Sartorius, Germany) using the Archimedes principle. NIH ImageJ

software was used to calculate the porosity percentage, relative density (100% - void percentage), and the percentage of unmelted Mo.

2.4 Mechanical Testing

Vickers microhardness tests were performed using a Struers DuraScan machine equipped with an automated indenter under a load of 100 g for 15 s per point. The groups of single crystal micropillars (2 μm diameters) were prepared using FIB operated at an ion beam voltage of 30 kV, along the <001> orientation of the β matrix. The uniaxial compression tests were performed using a Hysitron Ti-950 nanoindenter equipped with a 10 μm flat diamond tip, at a constant strain rate of 5×10^{-4}/s. Macro-compression tests (with the sample size of 3 mm × 3 mm × 7 mm) were conducted using an MTS CMT 5000 machine with a crosshead rate of 0.2 mm/min, following the ASTM E9-09 standard [37]. Digital image correlation (DIC) technology with a camera (Canon, Japan) recording was performed during compression tests. The obtained images were analysed using GOM correlate software (Zeiss, Germany). The tests were repeated three times to verify the reproducibility of the results.

3. Results and Discussion

First, the melting and homogenisation of refractory Mo particles during LPBF processing of a Ti-12Mo alloy as a function of laser energy input were investigated using a simple scanning strategy. When the optimal laser energy input was identified, the chess scan strategy was used to print the Ti-12Mo alloy; however, keyhole defects formed. The keyhole defects were largely eliminated by controlling LBD and IS settings. In addition, we produced a layered Ti-Mo FGC, of which the macro- and micro-mechanical properties, and the microstructures were

characterised in detail.

3.1. Melting and Homogenisation

To obtain Ti-Mo alloys with no unmelted Mo particles and ensure that Mo was homogeneously distributed, the LPBF parameters were optimised using a simple scan strategy, varying laser energy, scan speed and hatch spacing, as specified in Table 2. The corresponding AED was calculated according to Eq.1. Fig. 2a shows the BSE micrographs for the residual unmelted Mo powder within the builds with the increase of AED. The percentage of unmelted Mo was measured from the BSE images, which is plotted as a function of AED, as shown in Fig. 2b. The percentage of unmelted Mo decreased with an increase in AED from 1.3 to 4 J/mm^2. Then, the unmelted Mo particles reached an extremely low level ($\leq$ 0.15 %) when the AED was > 4 J/mm^2. This meant that the Mo particles were almost completely melted into the Ti matrix using LPBF with a high AED of 4 J/mm^2. The diffraction peaks of Mo was detected in the XRD patterns of the Ti-12Mo builds (Fig. 2c) at a laser AED of 1.7 J/mm^2, but such peaks disappeared at 4 J/mm^2, which indicate the melting and dissolution of Mo at 4 J/mm^2. The BSE image of Fig. 2d also shows no residual Mo particles.

The elemental distributions and chemical homogeneity of the Ti–12Mo alloy, prepared at 4 J/mm^2, were confirmed by EDS (Fig. 2e-f) and EPMA (Fig. 2h-i). The elemental maps were all taken from the middle of the sample. EDS elemental maps (Fig. 2e-f) show that Ti and Mo were distributed uniformly in the Ti-12Mo alloy, which accounted for 88.2 ($\pm$ 0.1) wt% and 11.8 ($\pm$ 0.1) wt%, respectively. In the previous study [2], a dense Ti-12Mo-6Zr-2Fe alloy was fabricated using the same in situ alloying based LBPF method. Some chemical inhomogeneity existed in the Ti-12Mo-6Zr-2Fe component at a large scale, although the average weight percentage of the elements was approximately the nominal content, similar to this present results. The BSE image (Fig. 2g) revealed the grain boundaries and melt pool boundaries of the Ti-12Mo alloy at a higher magnification. The corresponding EPMA elemental maps (Fig. 2h and i) show that a small amount of Mo segregated along the melt pool

boundaries, which are indicated by black arrows. The lowest and highest Mo concentrations were 7.84 wt% and 15.42 wt%, respectively.

The melt pool's microstructure was further examined for the builds with AEDs of 1.7, 2.2 and 4 J/mm^2. At a low AED of 1.7 J/mm^2, fish scale-like melt pools were observed with many unmelted Mo particles (Fig. 3a). Mo particles or Mo-riched regions were much brighter than the Ti matrix in the BSE image. Most of the coarse Mo particles were round, which indicated that those particles were hardly melted. There was some indication of Mo particles' melting, for example, irregular Mo particles and crescent-shaped Mo enriched areas. The crescent-shaped Mo enriched areas (pointed by the red arrows) were less bright than the round-shaped Mo particles. The areas' shapes and contrast suggested that these were the regions where Mo particles had been melted and mixed with Ti; however, they were not thoroughly homogenised. The residual Mo particles ' quantity was significantly lower at a higher AED of 2.2 J/mm^2 (Fig. 3b). Many irregulars or crescent-shaped Mo enriched areas (red arrows) and some partially melted Mo particles in a semicircular shape. At the AED of 4 J/mm^2 (Fig. 3c), no apparent residual Mo particles were observed. There was no prominent crescent-shaped Mo enriched area either.

Fig. 3d shows the sample's melt pool depth processed by an AED of 1.7 J/mm^2, which was 99.1 (± 5.6) µm. When the AED increased to 2.2 J/mm^2, the melt pool depth increased to be 181.6 (± 10.1) µm (Fig. 3e). The melt pool depth fabricated with an AED of 4 J/mm^2 was 379.0 (± 10.2) µm (Fig. 3f). The melt pool depth, which was the laser penetration depth, depended on the energy input and beam size, as well as the laser beam absorption, thermal conductivity and thermal diffusivity of the powder [38]. In this study, the melt pool depth depended on the AED value because the materials' physical properties and the laser beam size were the same for the three samples. The results showed a positive linear correlation between the AED and melt pool depth, as shown in Fig. S1, in good agreement with previous findings [39].

To manufacture a Ti-Mo alloy from Ti and Mo powders using LPBF, the first challenge that must be overcome is to melt the Mo particles. Mo has a very high melting temperature of

2,623°C. To melt the Mo particles in the blends, the melt pool temperature needed to reach over the melting point of Mo. However, due to lack of direct temperature monitoring of the melt pool in this study, the melt pool temperature could only be inferred from the melt pool characterisation. At a higher AED (e.g., 4 J/mm^2), the Mo particles were fully melted (no residual Mo, Fig. 2d). Some residual Mo particles were observed at a lower AED (e.g., 1.7 and 2.2 J/mm^2). However, some crescent-shaped Mo enriched areas (Fig. 3a and b, marked by red arrows) indicated melting of Mo, which suggests that the temperature in the melt pools was higher than the melting point of Mo particles during processing. The unmelted Mo particles were relatively large (> 23.3 ± 6.4 μm diameter) when AED is low (Fig. 3a and b), indicating that the coarse Mo particles require higher AED to melt entirely.

The second challenge for the in situ alloying LPBF processing of Ti-Mo alloys is to homogenise Mo into the Ti matrix. There are two methods to homogenise the powder layers during the in-situ alloying based LPBF. One uses the laser rescanning for each powder layer, as Brodie et al. [40] performed. The other uses extremely high energy input (up to 950w), as reported by Huang et al. [41]. In this work, we have investigated microstructural evolutions on Ti-Mo binary system with the energy input from low AED to high AED. The homogeneous microstructure was achieved via multiple remelts. During LPBF, each layer experiences multiple remelts from the laser beam, while the number of remelts depends on the melt pool depth. A constant powder layer thickness of 20 µm was used. The melt pool depths that used an AED of 1.7, 2.2 and 4 J/mm^2 were 99, 182 and 379 µm, respectively. Therefore, the remelt cycles of the three samples were estimated to be 5, 9 and 19, respectively. A higher AED of the laser significantly increased the number of remelts.

In a conventional arc melting process to cast Ti-Mo alloys, at least 5 remelts are applied to ensure homogenisation [2]. Fig. 3g schematically shows how multiple remelts can help the homogenisation of Mo. At a low AED of 1.7 J/mm^2, the melt pool was remelted 5 times. A large amount of Mo did not thoroughly mix into the Ti matrix, as shown in Fig. 3a and g. At a higher AED of 4 J/mm^2, the melt pool remelted approximately 19 times, which allowed Mo to fully

dissolve into the Ti matrix (Fig. 3c and g). Therefore, the homogenisation of Mo into the Ti matrix at a higher AED was attributed to the increased penetration depth, which enabled each layer to experience increased remelt cycles.

In summary, using a suitable high AED parameter, the laser beam could melt the refractory Mo particles into Ti and Mo powder blends and homogenise the composition. This would ensure the chemical homogenisation and mechanical repeatability in the Ti-12Mo component produced by the cost-effective LPBF in situ alloying.

3.2 Keyhole-induced Defects

When simple scanning was applied at an AED of 4 J/mm^2, no pores were found visually inside the specimens (Fig. 3c), and the relative density reached 99.99 (± 0.01) %. However, upon further increasing the AED to 5 J/mm^2, the relative density showed a slight decrease to 99.45 (± 0.03) %, due to the formation of keyhole pores, as demonstrated in Fig. S2.

The optimization of LPBF processing parameters via a simple scan strategy showed that, at an AED of 4 J/mm^2, Mo particles could be melted, and the composition was homogeneous. However, to manufacture large components, the simple scanning strategy results in high thermal residual stress which would increase cracking potential [42], due to the considerable scan track length and slower cooling rate [43]. To reduce the inner residual stress, it is necessary to use more advanced scanning strategies, such as chess scanning with a smaller scan track length [44]. However, when chess scanning was conducted at the AED of 4 J/mm^2, keyhole defects emerged, as shown in Fig. 4a. Some regions contain high-density keyholes, where the width is same to that of the island (5 mm). The spacing between the keyholes is mainly consistent. Thus, it is highly possible that the regions are located right on the edge position of two neighbour islands, due to the scanning traces are perpendicular between the adjoint islands. Fig. 4b shows the melt pool morphology on the top layer of the chess scanned Ti-12Mo alloy, which did not experience successive remelts. The keyhole defects were located at the bottom of the melt pool. Fig. 4c shows the melt pools, and pores in the middle layer of the chess scanned Ti-12Mo alloy. Some pores were observed at the bottom of the melt pools, while some

elongated pores crossed a few layers.

Keyhole defects are related to the laser energy input. If the laser energy is too high, large keyhole defects could form [24]. The formation mechanism for keyhole defects is shown in Fig. 4d. During the interaction between the laser beam and powder bed, holes generated at the bottom of the melt pool (Fig. 4b) after a single melt, where the highest energy was concentrated at the bottom of the melt pool [45]. This induced a temperature gradient from the bottom to the top of the melt pool. The laser beam penetrated deep into the material if sufficiently high energy was applied. In this case, the metal vaporised from the bottom of the melt pool, which could cause intense recoil pressure that would push the liquid metal away from the solid part [46]. Following solidification, pores were trapped at the bottom of the melt pool (Fig. 4c). If the laser energy was high enough to cause deep multiple remelts, beam penetration could repeatedly open the pore defects, which elongated the keyholes, as schematically shown in Fig. 4d.

Using the same AED of 4 J/mm^2, the keyhole-induced defects were observed in the samples processed by the chess scanning strategy (Fig. 4a), and also in the edge of the samples prepared using the simple scanning strategy with high LBD (Fig. S3a). In this study, low and high LBD values were set to 0.1 and 0.3 ms, respectively. The microstructure of the samples processed using the same parameters of chess scanning strategy, with varied LBD settings, have been compared (Fig. 5a and b). The melt pool shapes can be clearly observed. The deep melt pool can be seen from the start and end point of scanning trace in the high LBD sample (Fig. 5a). Some keyholes were also formed at the edge of islands. These findings indicate that the laser was dwelled at the start and end point of the scan trace before changing the laser vector (Fig. 5c). Due to the island shift (X + 1 mm and Y + 1 mm) and rotation (90º) for each layer, the keyholes were also found in some layers. These keyholes should be formed right on the edge of the neighbour island. The distance of the keyholes along the build direction, is about 200 µm, which is ten times the powders' layer thickness. This is because the island would move to the original position with the same scanning direction after ten shifts because of the island shift and rotation. The chess scan profile is also shown in Fig. 5d where the red lines indicate

scan traces. According to Fig. 5c, a higher dwelling time at the start (t1 to t2) and end (t5 to t6) of the scan path resulted in a higher laser energy input than that of the middle of the scan trace (which is the same as the simple scan used the same overall AED of 4 J/mm^2). Hence, the AED should be higher than 4 J/mm^2 during dwelling, accelerating and slowing down of laser beam. As we stated before, when AED was increased to 5 J/mm^2 for simple scan, pores defects also formed. Therefore, keyhole defects formed at the start and end of the scan paths.

Due to the high AED applied in this work, the formation of keyholes is sensitive to the LBD setting. Although the time to achieve final velocity is short, a bit more delaying (0.2 ms) of dwelling time can induce higher heat concentrations. To eliminate keyhole defects formed during the chess scanning, the optimisation of LBD and IS settings were possible solutions. As shown in Fig. 5e, the IS could be described as the compensation of adjacent islands to obtain the adequate overlap between the neighbouring islands (marked by green circles in Fig. 5d). Comparing the relative density of the chess scanned samples with high and low LBD settings, a low LBD could produce samples of high relative density (≥ 99.7%), regardless of the IS (Fig. 5f). The LBD setting influenced the melt pool's penetration depth [46], whereby lower LBD led to shallower melt pools at the ends of the scan trace (Fig. 5b and c) that had a lower potential to generate keyhole-induced defects. However, at a higher LBD, IS settings had a strong influence on the relative density. At low IS values, the relative density was low, which indicated the formation of keyhole defects. When the IS was 0.105 mm, the relative density of the print was 99.1 %. The relative density increased to 99.98% with the decrease of IS from 0.15 to –0.45 mm, which indicated that keyhole defects were eliminated. With suitable IS settings (0.06 mm), the vapour in the keyhole had time to escape from the melt pool before solidification, and the melt pool was not deep enough to create new pores at the start and end of the scan trace, which allowed the keyholes to close during subsequent remelting. However, the samples cracked when the absolute value of IS settings was too high (≥ 0.45 mm), as shown in Fig. S4, which indicated that the high LBD and IS might increase the local inner stresses.

In summary, when laser AED was too high (e.g., > 4.4 J/mm^2), keyholes defects can be

formed. During chess scanning, the laser beam is dwelling before accelerating, and after slowing down, then its velocity is lower at the two ends of the scanning trace; therefore, the AED was higher. When an AED of 4 J/mm^2 was used for the chess scan, the AED at the start and end of the scan trace was much higher than that in the middle, then the keyhole defects formed at the boundaries of the chess islands. Thus, reducing the LBD settings helped to eliminate the keyholes. Additionally, an relatively high IS could consolidate the keyholes via remelting and refilling, in particular, for high LBD settings. Therefore, the LPBF processing parameters of 4 J/mm^2 AED with a low LBD of 0.1 ms and the IS value of 0.06 mm, can be used to fabricate dense Ti-12Mo components with high relative density (> 99.9 %).

3.3 Microstructure of the Ti-12Mo Alloy

The microstructures of Ti-Mo samples were compared with varied AEDs. The samples processed by low AED (1.6 J/mm^2) and high AED (4 J/mm^2) were named low energy (LE) and high energy (HE) specimens, respectively. The processing parameters are given in Table 3. For the LE sample, the XRD pattern in Fig. 6a revealed the body-centred cubic (BCC) β and orthorhombic α" phase inside the LE sample, as well as the peaks of Mo. Fig. 6b shows the coarse residual Mo particles inside the LE sample, which were partially melted. As shown in Fig. 6c, high-density fine α" plates were seen in the LE samples. For the HE specimen, XRD shown in Fig. 6d mainly illustrates the β phase and some ω phase, whereas the α" phase was limited. A few small Mo particles were found in the HE samples, as shown in Fig. 6e. Under higher magnification (Fig. 6f), no α" phase was observed in the BSE image. Comparing HE and LE samples, it was concluded that the amount of residual Mo particles and the phase constitutes were different between the two sets of specimens.

3.4 Fabrication of the Ti-Mo FGC

As shown, different Mo and phase contents can be obtained using different AED. Following this, a Ti-Mo FGC was designed with a layered composite structure that alternated

the energy inputs, as shown in Fig. 7a. The matrix was produced by high energy input at 4 J/mm^2, designated as HE input layers. Two layers were printed using LE, designed with a thickness of 0.5 mm each, in the middle of the HE matrix. The detailed LPBF processing parameters of LE and HE layers were the same as that of the LE and HE samples, respectively (Table 3). As shown in Fig. 7b, the Ti-Mo FGC is near fully dense, with only a few minor defects. The unmelted Mo particles were found in the LE layer, and only a few unmelted Mo particles were observed in the HE matrix. Fig. 7c and d show the inhomogeneous distributions of Ti and Mo solute elements along the build direction (BD). In the HE layers, Ti and Mo appeared to be homogeneously distributed. In the LE layers, Mo is still alloying into Ti, although the fraction was lower than that of the HE layers because some Mo particles were unmelted.

3.5 Microstructure of the Ti-Mo FGC

To reveal the microstructure of the Ti-Mo FGC, EBSD was performed in the interdiffusion area between the HE and LE layers, as indicated by the transparent yellow square shown in Fig. 7b. The inverse pole figure (IPF) map (Fig. 8a) shows the grain structure of β phase, which became coarser from the LE to HE area. In addition, the local misorientation decreased from the LE to HE areas steadily, as illustrated in the kernel average misorientation (KAM) map (Fig. 8b), which represents the density of geometrically necessary dislocations (GNDs) [47]. The higher KAM values mean a higher density of GNDs stored. Then, it shows higher stress concentrations when closer to the LE layers. As shown in Fig. 8c, the main phase across the boundary was the β phase. However, α" phase was heterogeneously distributed along the build direction across the interface. Almost no α" phase was found in the HE layers at this resolution, and the amount of α" phase increased from the HE to LE side. The α" phase changed across the interface, and its size and distributions showed gradient distributions (Fig. 8g-i). The fine and dense α" particles in the LE areas (Fig. 8i) became coarser and sparser when they approached the HE area (Fig. 8h). Then, there was no apparent α" phase in the HE area (Fig. 8g).

The elemental distribution mapping and points scanning results (Fig. 8d–f) revealed the

detailed distributions of Mo, the β stabiliser. Mo concentration was higher in the area closer to the HE layers and gradually decreased in the region close to the LE layer. This variation of Mo contents substantially influenced the phase constituents in Ti-Mo binary alloys [48]. In addition, the microstructure of the interdiffusion area from HE to LE on the other side is shown in Fig. S5, where the melt pool depth changed from deep to shallow. During the LPBF processing, each layer remelted several times. The melt pool depth of the LE layers was 100 ± 11 μm, according to Fig. S6. Therefore, there were 5 remelts for the LE areas, in contrast to 19 remelts for the HE layers. The remelting times play a vital role in dissolving Mo into the Ti matrix (Fig. 3a-c). Therefore, the Mo content was lower in the LE layer, which experienced fewer remelts.

In addition, the detailed microstructures in the HE and LE areas were characterised by TEM. The FIB lamellar was lifted out across a grain boundary inside the HE area (Fig. 9a). It is found that the nanosized α" phases were located along the grain boundaries (Fig. 9b). Bright-field TEM micrograph (Fig. 9c) illustrates the high-density black ellipses. The selected area electron diffraction (SAED) pattern along the $[\bar{1}13]_{\beta}$ zone axis shows diffraction spots of ω phases, which were of high intensity without diffuse streaks. This indicated the high-density ω phases in the HE area. The dark-field TEM images (Fig. 9d and e) revealed the morphology of the ω phases with two different orientations, ω1 and ω2, which were collected from the SAED pattern (Fig. 9c). Although the $[\bar{1}13]_{\beta}$ zone axis was not perpendicular to the displacement vector of the B and C planes of β phase; it was appropriate to differentiate ω phases region, particularly for the dark-field TEM images.

Another FIB lamella was lifted out from the LE area of the Ti-Mo FGC (marked in Fig. 10a). Fig. 10b shows the bright-field TEM micrograph of a region in the FIB lamellar, observed along the $[111]_{\beta}$ zone axis. High-density plate-like α" phases were observed. The burgers orientation relationship (BOR) between the β and α" follows $[111]_{\beta}//[\bar{1}10]_{\alpha"}$ (Fig. 10c). The same BOR was reported in a previous study [49]. A bright-field TEM image (Fig. 10d) obtained from another region shows another BOR of $[111]_{\beta}//[101]_{\alpha"}$ (Fig. 10e). This BOR has also been reported previously [50]. The lattice parameters of orthorhombic α" phases were calculated

based on the SAED patterns, with *a*, *b* and *c* of 3.07, 5.18 and 4.69 Å, respectively, which were close to those (*a* = 2.99, *b* = 5.05 and *c* = 4.67 Å) in the Inorganic Crystal Structure Database (No. 253845) [51]. The microstructure was composed of plate-like α" phases and thin β films between the α" plates (Fig. 10f-h). The α" phase was enriched with Ti, and the β phase has small quantities of Ti and was rich in Mo.

In the Ti-Mo binary alloy system, the secondary phases' constitution in the quenched (over β transus) sample depends on the Mo content [49]. With an increase in Mo content, the martensite structure is obtained during fast cooling or from low-temperature ageing treatment, which changed from hexagonal (α') to orthorhombic (α") when 4 wt% was reached [52]. The structure became the β phase when Mo was close to or >10 wt%. During laser remelting, with fast heating and a cooling rate (≤ 10^7 °C/s), the approximately fully β phase matrix could be fully retained at about 9 wt% Mo content (Fig. 8g). The coarse and sparse α" phases formed in the middle area when Mo content was approximately 6 wt%. The much finer α" phases formed in the area with a close concentration, around 7 wt% Mo. Therefore, the Mo concentrations increased from approximately 6 wt% to 9 wt% across the interdiffusion region, which played an essential role in determining the fraction and morphology of the α" phase in the FGC. In addition, the diffusion between the HE and LE layers could influence the precipitation of the α" phases, due to the deep melt pool depth, which penetrated from the HE to LE layers (Fig. 8j).

3.6 Macro and Micro Mechanical Behaviours.

Fig. 11 shows the Vickers microhardness evolutions along the build direction, which cross the HE and LE layers, as shown in Fig. 7b. The results show that the microhardness was much higher in the HE layers than in the LE layers. The average microhardness in the LE was 410 (± 23) HV. For the HE layers, the microhardness results varied from the region between the LE layers and the region outside the middle area, where the average microhardness was 461 (± 13) HV and 508 (± 18) HV, respectively. The microhardness variation in the two HE regions might be due to the different thermal histories experienced during fabrication.

Fig. 12a shows the macro compressive stress-strain curves of the Ti-Mo FGC, LE and HE samples. The strains were measured by digital image correlation. The evolution and distribution of local strain can be seen in Fig. S7. The dynamic evolution of the strain distributions of the samples during compression are in the supplementary videos. In addition, the development of strain hardening rates is shown in Fig. 12b. The Ti-Mo FGC illustrated the best compression mechanical behaviours compared with the LE or HE samples. The LE samples show the lowest yield strength of 843 (± 22) MPa, and they possessed the highest work hardening rate during deformation. The HE samples illustrated a higher yield strength of 1168 (± 24) MPa, although no apparent work hardening capacity, particularly in the early stage of plastic deformation. Following the introduction of two LE layers, the Ti-Mo FGC presented a slightly higher yield strength of 1173 (± 15) MPa, and significantly improved strain hardening rate, demonstrating better compression behaviour.

To study the mechanical performance of the matrix, avoiding the impacts from grain boundaries, crystallographic orientations, and residual Mo particles, single crystal micropillars were milled from the β grains with <001> orientation in the LE and HE layers. The single crystal micropillars in LE and HE layers were composed of β matrix + α" precipitates and β matrix + ω precipitates respectively, according to Fig.9 and Fig.10. Micropillar compression tests were carried out at room temperature. The typical stress-strain curves are shown in Fig. 13a. The curve is smooth and continuous for the micropillars from the LE layer, and no strain bursts were observed. The yield strength was 1483 (± 24) MPa. Strain hardening behaviour was observed. The stress-strain curve obtained from the micropillars taken from the HE layers showed significant strain bursts during deformation, different from that of the LE layer. The yield strength was 1301 (± 16) MPa. Fig. 13b-d shows the morphology of LE micropillars before and after the compression tests. The tortuous slip traces were observed from the surface of the deformed micropillars (Fig. 13d) instead of a normal slip band. Fig. 13e-g show the morphology of HE micropillars before and after the compression test. The parallel slip bands were observed on the HE layers micropillars' surface (Fig. 13g), which meant that the same slip

system with fine slip steps was activated during compression.

3.7 Post-deformation characterization

Fig. 14 illustrated the microstructures of the deformed HE layers of the FGC sample. Some slip traces are observed inside the FIB lamellar marked by the dotted lines, as shown in Fig. 14a. There are only β and ω phases revealed in the FIB lamella, and slip traces are along the $\{11\bar{2}\}<111>$ slip system, according to the SAED pattern in Fig.14b. Inside the slip traces, the dislocations are visible. As illustrated in Fig.14c, the slip traces were ω free channels, suggesting the ω → β phase transformation during the compression tests [53]. The BOR between the hexagonal ω and BCC β phases is following $[11\bar{2}0]_{\omega}$ //$[\bar{1}10]_{\beta}$ and $(0001)_{\omega}$//$(111)_{\beta}$ [54]. Then $\{\bar{1}100\}_{\omega}$, the prismatic slip plane of ω phase, is parallel to the $\{11\bar{2}\}_{\beta}$, which is corresponding with the activated slip plane [55]. Due to the coherence phase boundaries between the β and ω phases, it is much easier for the coherent slip planes to transfer from $\{11\bar{2}\}_{\beta}$ to $\{\bar{1}100\}_{\omega}$ planes [56]. Therefore, the dislocations move and shear the ω phases during the deformation, forming the ω phases free channels in the slip traces. These channels reduce the resistance for dislocations to move, which made the plastic flow localised and then boost the movement of dislocations along the traces. Therefore, the strain bursts happened as observed in the micropillar compression test of the HE sample. This phenomenon can be account for the low strain hardening capacity. Although the ω phase is well-known to significantly strengthen the β Ti alloys due to its high shear modulus [57], the micro compression tests show limited strength. Obviously, there was no obstruction from the grain boundaries during the deformation of the single-crystal micropillars with β + ω phases. Thus, the significant strain burst can frequently occur during the deformation, which limited the strength of micropillars.

In LE layers, the microstructure is composed of β, multiple α" variants and some crescent Mo particles. These Mo particles may be surrounded by the transitional phases' composition of α', α" or α depends on the localised Mo concentrations [13]. Fig. 15 shows the microstructure

of the deformed LE layers (without Mo particles), which were composed of β and α" phases before the compression. As shown in Fig. 15b, the SAED pattern illustrates that the α" variant is aligned with the $[111]_{\alpha"}$ zone axis. The high-density dislocations can be observed in Fig. 15c, which were found in all α" grains. Therefore, the multi variants of α" and the interfaces between α" and the matrix can impede the continuous movement of dislocations during deformation. And the deformable α" phases show great storage capability of high-density dislocations. The orthorhombic α" is an intermediate phase between the BCC β and HCP α, of which the transformation of β → α" should require much smaller principal strains than that of β → α [52]. After compression, the β matrix phase (Fig. 10f-h) was not observed, suggesting the martensite phase transformation of β → α" might occur. Therefore, due to the trapping of dislocations by α" phases, and the possible martensite phase transformation during deformation, the high strength and strain hardening rate are obtained for micropillars in the LE layers.

The α" phases rich layers (LE) can act as the role of the barriers and sinks to the dislocations (Fig. 15c), which is similar to the α phase [55, 58]. After introducing the two LE layers with rich α" to the HE samples, the dislocations' accumulation and interaction are enhanced, providing an obvious strain hardening rate up-turn in the FGC materials. With both β + ω and β + α" structures in FGC materials, high strength and high strain hardening rate were obtained. Such mechanical performance is inherent to FGC materials, and does not exist in homogeneous materials (HE or LE).

The LE samples show high strength in single-crystal micropillars, while low strength in macro compressive tests. One reason is the size effect of the β + α" structure [58, 59]. Thereby, the LE samples can follow the "smaller is stronger". Another one is the effects of the unmelted Mo particles in LE samples, which might be detrimental to the strength of LE macro samples. Future work is needed to reveal the strengthening effects from undissolved Mo particles in such complicated microstructure.

4. Outlook and Challenges

FGCs have several potential applications in structural and functional applications, and the increase in AM will significantly accelerate the development of metallic FGCs. However, their fabrication methods and control mechanisms require further investigations [22]. Several studies have shown that fabricating using different alloy gradients could lead to severe defects [30], due to various thermophysical properties. The rules for the material selection of FGCs have not been systematically investigated. In addition, the optimisation of parameters for laser processing is critical to forming highly dense FGCs by AM. The blends contained particles with different thermophysical properties, and the influence of the size, distribution and content of the residual particles on the mechanical properties of solid samples remains undetermined [2]. In this study, the size and content of refractory particles in the matrix were successfully controlled by tailoring the scanning parameters of the LPBF to obtain highly dense Ti-Mo FGCs. Different laser scanning parameters and strategies could significantly influence the solute concentrations and the thermal history of the processing, which could result in a gradient distribution of the precipitated phase composition, as shown in this study. More in-depth studies are required to achieve precise control of the microstructure of FGCs. Finally, the inhomogeneity, as well as the reproducibility of the components, from batch to batch, constitutes a major challenge due to the random nature of the powder quality and the particle size distributions. Therefore, further work is required to ensure quality control before the industrial applications of FGCs prepared by AM.

5. Conclusions

By exploring the relationship between the scanning parameters and the corresponding microstructure, the promising approach of in situ based LPBF alloying has been demonstrated to produce a near fully dense Ti-12Mo alloy and its FGC, which has a combination of high strength and excellent strain hardening behaviour. The key findings were summarized as follows:

(1) Mo particles melted and dissolved into the Ti matrix using high laser energy input (4 J/mm^2),

which was attributed to repeated remelts. Keyhole-induced defects formed due to excessively high HE input could be eliminated by optimising the LBD and IS settings of LPBF processing. By applying the optimised parameters of 4 J/mm^2 AED, with low LBD and IS values of 0.1 ms and 0.06 mm, the highly dense (> 99.9%) Ti-12Mo alloy could be fabricated.

(2) During LPBF in situ alloying of Ti-12Mo, the input energy density significantly influenced the specimen's microstructure, including the grain structures, the inner stress, and the phases constitutions. At an AED of 1.6 J/mm^2, the microstructure contained refined grains, high inner stress and β + α" phases. At an AED of 4 J/mm^2, the microstructure consisted of the larger grains and reduced inner stress, where the phases constitutions were mainly β and ω phases, with a small amount of α" phase along the grain boundaries. The grain, composed of β and α" phases, showed high strength and large strain hardening capacity. In contrast, the grain with β and ω phases showed substantial strain bursts without apparent strain hardening.

(3) The highly dense Ti-Mo FGCs were successfully prepared by controlling the energy input for the LPBF processing of the powder blends. The Ti-Mo FGCs illustrated a high yield strength of 1173 (± 15) MPa, with substantially improved strain hardening capacity at the early stage of plastic deformation. This finding opens a new opportunity to design and engineer biomimetic FGCs using LPBF in situ alloying from powder blends.

Author Credits

Ranxi Duan: Conceptualization, Methodology, Investigation, Formal analysis, Data curation, Validation, Visualization, Writing-original draft; **Sheng Li**: Investigation, Methodology, Validation; **Biao Cai**: Supervision, Conceptualization, Validation, Writing-review & editing; **Zhi Tao**: Investigation; **Weiwei Zhu**: Investigation; **Fuzeng Ren**: Supervision, Conceptualization, Project administration, Resources, Writing-review & editing; **Moataz M. Attallah** : Supervision, Project administration, Resources, Writing-review &

editing.

Acknowledgments

This work was financially supported by the Fundamental Research Program of Shenzhen (Grant No. JCYJ20170412153039309), and Guangdong Innovative & Entrepreneurial Research Team Program (No. 2016ZT06C279). This work was also supported by the Pico Center at SUSTech that receives support from Presidential fund and Development and Reform Commission of Shenzhen Municipality. B.C. acklowdges the funding support from the Royal Society (No. RGS\R2\202122 and IEC\NSFC\191319).

Declaration of interests

The authors declare that they have no known competing financial interests or personal relationships that could have appeared to influence the work reported in this paper.

Appendix A. Supplementary Material contains Fig. S1-S7.

References:

[1] Leyens C, Peters M. Titanium and titanium alloys: fundamentals and applications. New York: Wiley-VCH; 2003.

[2] Duan R, Li S, Cai B, Zhu W, Ren F, Attallah MM. A high strength and low modulus metastable β Ti-12Mo-6Zr-2Fe alloy fabricated by laser powder bed fusion in-situ alloying. Addit Manuf. 2020:101708.

[3] Sun F, Zhang JY, Marteleur M, Gloriant T, Vermaut P, Laillé D, et al. Investigation of early stage deformation mechanisms in a metastable β titanium alloy showing combined twinning-induced plasticity and transformation-induced plasticity effects. Acta Mater. 2013;61(17):6406 - 17.

[4] Zhu L, Zhang Q, Chen Z, Wei C, Cai G-M, Jiang L, et al. Measurement of interdiffusion

and impurity diffusion coefficients in the bcc phase of the Ti–X (X = Cr, Hf, Mo, Nb, V, Zr) binary systems using diffusion multiples. J Mater Sci. 2016;52(6):3255 - 68.
[5] Ho WF, Ju CP, Chern Lin JH. Structure and properties of cast binary Ti–Mo alloys. Biomaterials. 1999;20(22):2115-22.
[6] Sing SL, Yeong WY, Wiria FE. Selective laser melting of titanium alloy with 50 wt% tantalum: Microstructure and mechanical properties. J Alloys Compd. 2016;660:461-70.
[7] DebRoy T, Wei HL, Zuback JS, Mukherjee T, Elmer JW, Milewski JO, et al. Additive manufacturing of metallic components – Process, structure and properties. Prog Mater Sci. 2018;92:112-224.
[8] Veeck S, Lee D, Boyer R, Briggs R. The castability of Ti-5553 alloy: Its microstructure and properties. J Adv Mater. 2005;37(4):40-5.
[9] Niu J, Dai G, Guo Y, Sun Z, Dan Z, Dong Y, et al. Microstructure and mechanical properties of B modified Ti–Fe alloy manufactured by casting, forging and laser melting deposition. Compos Part B Eng. 2021;216:108854.
[10] Zhang LC, Klemm D, Eckert J, Hao YL, Sercombe TB. Manufacture by selective laser melting and mechanical behavior of a biomedical Ti–24Nb–4Zr–8Sn alloy. Scr Mater. 2011;65(1):21-4.
[11] Ishimoto T, Hagihara K, Hisamoto K, Sun S-H, Nakano T. Crystallographic texture control of beta-type Ti–15Mo–5Zr–3Al alloy by selective laser melting for the development of novel implants with a biocompatible low Young's modulus. Scr Mater. 2017;132(C):34 - 8.
[12] Zhou Z, Liu Y, Liu X, Zhan Q, Wang K. Microstructure evolution and mechanical properties of in-situ Ti6Al4V–TiB composites manufactured by selective laser melting. Compos Part B Eng. 2021;207:108567.
[13] Vrancken B, Thijs L, Kruth JP, Humbeeck JV. Microstructure and mechanical properties of a novel β titanium metallic composite by selective laser melting. Acta Mater. 2014;68:150-8.
[14] Fang M, Han Y, Shi Z, Huang G, Song J, Lu W. Embedding boron into Ti powder for direct laser deposited titanium matrix composite: Microstructure evolution and the role of nano-TiB network structure. Compos Part B Eng. 2021;211:108683.
[15] Zhai W, Zhu Z, Zhou W, Nai SML, Wei J. Selective laser melting of dispersed TiC particles strengthened 316L stainless steel. Compos Part B Eng. 2020;199:108291.
[16] Han Q, Gu Y, Huang J, Wang L, Low KWQ, Feng Q, et al. Selective laser melting of Hastelloy X nanocomposite: Effects of TiC reinforcement on crack elimination and strength improvement. Compos Part B Eng. 2020;202:108442.
[17] Liu S, Han S, Zhang L, Chen L-Y, Wang L, Zhang L, et al. Strengthening mechanism and micropillar analysis of high-strength NiTi–Nb eutectic-type alloy prepared by laser powder bed fusion. Compos Part B Eng. 2020;200:108358.
[18] Yang Y, Yang M, He C, Qi F, Wang D, Peng S, et al. Rare earth improves strength and creep resistance of additively manufactured Zn implants. Compos Part B Eng. 2021;216:108882.
[19] Mosallanejad MH, Niroumand B, Aversa A, Saboori A. In-Situ Alloying in Laser-Based Additive Manufacturing Processes: A Critical Review. J Alloys Compd. 2021;872:159567.
[20] Sing SL, Huang S, Goh GD, Goh GL, Tey CF, Tan JHK, et al. Emerging Metallic Systems for Additive Manufacturing: In-situ Alloying and Multi-metal Processing in Laser Powder Bed

Fusion. Prog Mater Sci. 2021:100795.
[21] Meng X, Min J, Sun Z, Zhang W, Chang H, Han Y. Columnar to equiaxed grain transition of laser deposited Ti6Al4V using nano-sized B4C particles. Compos Part B Eng. 2021;212:108667.
[22] Zhang J, Song B, Yang L, Liu R, Zhang L, Shi Y. Microstructure evolution and mechanical properties of TiB/Ti6Al4V gradient-material lattice structure fabricated by laser powder bed fusion. Compos Part B Eng. 2020;202:108417.
[23] Palik E. Handbook of Optical Constants of Solids. 1997:xv-xvi.
[24] Cunningham R, Zhao C, Parab N, Kantzos C, Pauza J, Fezzaa K, et al. Keyhole threshold and morphology in laser melting revealed by ultrahigh-speed x-ray imaging. Science. 2019;363(6429):849-52.
[25] Zhao C, Guo Q, Li X, Parab N, Fezzaa K, Tan W, et al. Bulk-Explosion-Induced Metal Spattering During Laser Processing. Phys Rev X. 2019;9(2):021052.
[26] Hirano K, Fabbro R, Muller M. Experimental determination of temperature threshold for melt surface deformation during laser interaction on iron at atmospheric pressure. J Phys D: Appl Phys. 2011;44(43):435402.
[27] Mazumder J, Ki H, Mohanty PS. Role of recoil pressure, multiple reflections, and free surface evolution during laser keyhole welding. In: Proceedings of ICALEO 2002 - 21st International Congress on Applications of Laser and Electro-Optics, Congress Proceedings. Conference Dec 01, Conference 2002.
[28] Zhao C, Parab ND, Li X, Fezzaa K, Tan W, Rollett AD, et al. Critical instability at moving keyhole tip generates porosity in laser melting. Science. 2020;370(6520):1080-6.
[29] Zhai W, Wang P, Ng FL, Zhou W, Nai SML, Wei J. Hybrid manufacturing of γ-TiAl and Ti–6Al–4V bimetal component with enhanced strength using electron beam melting. Compos Part B Eng. 2021;207:108587.
[30] Naebe M, Shirvanimoghaddam K. Functionally graded materials: A review of fabrication and properties. Appl Mater Today. 2016;5:223-45.
[31] Wu X, Jiang P, Chen L, Yuan F, Zhu YT. Extraordinary strain hardening by gradient structure. P Natl Acad Sci USA. 2014;111(20):7197-201.
[32] Ma X, Li F, Sun Z, Hou J, Fang X, Zhu Y, et al. Achieving Gradient Martensite Structure and Enhanced Mechanical Properties in a Metastable β Titanium Alloy. Metall Mater Trans A. 2019;50(5):2126-38.
[33] Krakhmalev P, Yadroitsava I, Fredriksson G, Yadroitsev I. In situ heat treatment in selective laser melted martensitic AISI 420 stainless steels. Mater Design. 2015;87:380-5.
[34] Kürnsteiner P, Wilms MB, Weisheit A, Gault B, Jägle EA, Raabe D. High-strength Damascus steel by additive manufacturing. Nature. 2020;582(7813):515-9.
[35] Spierings AB, Voegtlin M, Bauer T, Wegener K. Powder flowability characterisation methodology for powder-bed-based metal additive manufacturing. Prog Addit Manuf. 2016;1(1-2):9-20.
[36] Carter LN, Essa K, Attallah MM. Optimisation of selective laser melting for a high temperature Ni-superalloy. Rapid Prototyp J. 2015;21(4):423-32.
[37] E9-09 A. Standard Test Methods of Compression Testing of Metallic Materials at Room Temperature. West Conshohocken, PA: ASTM International; 2009.
[38] Rubenchik AM, King WE, Wu SS. Scaling laws for the additive manufacturing. J Mater

Process Technol. 2018;257:234 - 43.
[39] Trapp J, Rubenchik AM, Guss G, Matthews MJ. In situ absorptivity measurements of metallic powders during laser powder-bed fusion additive manufacturing. Appl Mater Today. 2017;9:341-9.
[40] Brodie EG, Medvedev AE, Frith JE, Dargusch MS, Fraser HL, Molotnikov A. Remelt processing and microstructure of selective laser melted Ti25Ta. J Alloys Compd. 2020;820:153082.
[41] Huang S, Narayan RL, Tan JHK, Sing SL, Yeong WY. Resolving the porosity-unmelted inclusion dilemma during in-situ alloying of Ti34Nb via Laser Powder Bed Fusion. Acta Mater. 2020;204:116522.
[42] Gibson I, Rosen DW, Stucker B. Additive Manufacturing Technologies. 2010.
[43] Ali H, Ghadbeigi H, Mumtaz K. Effect of scanning strategies on residual stress and mechanical properties of Selective Laser Melted Ti6Al4V. Mater Sci Eng, A. 2018;712(226):175-87.
[44] Carter LN, Martin C, Withers PJ, Attallah MM. The influence of the laser scan strategy on grain structure and cracking behaviour in SLM powder-bed fabricated nickel superalloy. J Alloys Compd. 2014;615:338-47.
[45] Liu YJ, Li SJ, Wang HL, Hou WT, Hao YL, Yang R, et al. Microstructure, defects and mechanical behavior of beta-type titanium porous structures manufactured by electron beam melting and selective laser melting. Acta Mater. 2016;113:56-67.
[46] Semak V, Matsunawa A. The role of recoil pressure in energy balance during laser materials processing. J Phys D: Appl Phys. 1997;30(18):2541-52.
[47] Kumar SSS, Pavithra B, Singh V, Ghosal P, Raghu T. Tensile anisotropy associated microstructural and microtextural evolution in a metastable beta titanium alloy. Mater Sci Eng, A. 2019;747:1-16.
[48] Sochacka P, Miklaszewski A, Jurczyk M. The Influence of Mo Content on Phase Transformation in Ti-Mo Alloys. Arch Metall Mater. 2017;62(4):2051-6.
[49] Wang CH, Yang CD, Liu M, Li X, Hu PF, Russell AM, et al. Martensitic microstructures and mechanical properties of as-quenched metastable β-type Ti–Mo alloys. J Mater Sci. 2016;51(14):6886-96.
[50] Wang L, Fu C, Wu Y, Li R, Hui X, Wang Y. Superelastic effect in Ti-rich high entropy alloys via stress-induced martensitic transformation. Scr Mater. 2019;162:112 - 7.
[51] Sabeena M, Murugesan S, Anees P, Mohandas E, Vijayalakshmi M. Crystal structure and bonding characteristics of transformation products of bcc β in Ti-Mo alloys. J Alloys Compd. 2017;705:769-81.
[52] Davis R, Flower HM, West DRF. Martensitic transformations in Ti-Mo alloys. J Mater Sci. 1979;14(3):712-22.
[53] Chen W, Zhang J, Cao S, Pan Y, Huang M, Hu Q, et al. Strong deformation anisotropies of ω-precipitates and strengthening mechanisms in Ti-10V-2Fe-3Al alloy micropillars: Precipitates shearing vs precipitates disordering. Acta Mater. 2016;117:68-80.
[54] Zháňal P, Harcuba P, Šmilauerová J, Stráský J, Janeček M, Smola B, et al. Phase Transformations in Ti-15Mo Investigated by in situ Electrical Resistance. Acta Phys Pol A. 2015;128(4):779-83.
[55] Kou W, Sun Q, Xiao L, Sun J. Superior plasticity stability and excellent strength in Ti-

55531 alloy micropillars via harmony slip in nanoscale α/β phases. Sci Rep-uk. 2019;9(1):5075.
[56] Ohmori Y, Ogo T, Nakai K, Kobayashi S. Effects of ω-phase precipitation on β→α, α″ transformations in a metastable β titanium alloy. Mater Sci Eng, A. 2001;312(1-2):182-8.
[57] Lai MJ, Li T, Yan FK, Li JS, Raabe D. Revisiting ω phase embrittlement in metastable β titanium alloys: Role of elemental partitioning. Scr Mater. 2021;193:38-42.
[58] Pan Y, Sun Q, Xiao L, Ding X, Sun J. Plastic deformation behavior and microscopic mechanism of metastable Ti-10V-2Fe-3Al alloy single crystal pillars orientated to <011>β in submicron scales Part I: Double size effects and martensitic transformation prediction. Mater Sci Eng, A. 2019;743:798-803.
[59] Kou W, Sun Q, Xiao L, Sun J. Coupling effect of second phase and phase interface on deformation behaviours in microscale Ti-55531 pillars. J Alloys Compd. 2020;820:153421.

Tables:

Table 1 Characteristics of pure Ti and Ti-12Mo blended powders.

	Apparent density (g/cm^3)	Tap density (g/cm^3)	F.F.C.	Hausner ratio
Ti	2.2 ± 0.001	2.6 ± 0.01	19.0 ± 1	1.2 ± 0.006
Ti-12Mo	2.5 ± 0.03	3.0 ± 0.002	22.5 ± 0.4	1.2 ± 0.01

Table 2 Scanning parameters of the Ti-12Mo alloy using LPBF.

No.	Laser power (w)	Scan speed（mm/s）	Hatch spacing (mm)	Linear energy density (J/mm)	Area energy density（J/mm^2）
1	250	2500	0.075	0.10	1.3
2	200	2000	0.06	0.10	1.7
3	250	1500	0.075	0.17	2.2
4	300	1000	0.075	0.30	4
5	200	1000	0.045	0.20	4.4
6	300	1000	0.06	0.30	5

Table 3 Scanning parameters of the Ti-Mo FGC using LPBF.

Ti-Mo	Laser power (w)	Scan speed (mm/s)	Hatch spacing (mm)	Island size (mm×mm)	Area energy density (J/mm^2)
LE	120	1000	0.075	5×5	1.6
HE	300	1000	0.075	5×5	4

Figure captions:

Fig. 1. (a) The particle size distributions of Ti and Mo elemental powders; (b) the schematic of the powder blending process; (c) BSE micrograph of Ti-12Mo blended powder; (d) the schematic of LPBF in situ alloying processing; (e) as-fabricated samples with different scanning parameters; and (f) schematic illustration of the scanning strategies depicting the island spacing, and beam delay settings.

Fig. 2 (a) BSE images of as-fabricated Ti-12Mo specimens (values on the images are the AED); (b) effect of AED on the percentage of un-melted Mo and density; (c) XRD patterns of as-fabricated Ti-12Mo cube specimens; (d) BSE micrograph of Ti-12Mo sample; (e) and (f) are EDS elemental maps of Ti and Mo, respectively; (g) high magnification BSE micrograph (black dotted lines indicated the melt pool boundaries); (h) and (i) are the EPMA maps of Ti and Mo, respectively.

Fig. 3. (a)–(c) are BSE micrographs of the as-fabricated Ti-12Mo sample under different processing conditions: (a) low AED (1.7 J/mm^2), (b) middle AED (2.2 J/mm^2) and (c) high AED (4 J/mm^2); (d) and (e) are the side-view BSE images of the top layer of the samples fabricated using the AED of 1.7 and 2.2 J/mm^2, respectively; (f) the side-view optical micrograph of the top layer of the sample fabricated using AED of 4 J/mm^2; (g) the schematic illustration shows the remelting process of Mo particles during LPBF.

Fig. 4. (a) Optical micrograph of the full side section of the chess-scanned Ti-12Mo sample fabricated using AED of 4 J/mm^2, and high LBD settings; (b) and (c) are side-view optical micrographs of the keyholes of the chess-scanned Ti-12Mo alloy: (b) top layer; and (c) middle layer; and (d) the schematic illustration of the formation of keyholes defects.

Fig. 5. The OM images of the specimens processed using chess scanning strategy with high LBD (a) and low LBD (b), respectively (Red lines indicate the scanning directions of the top layer, the white lines present some melt pool boundaries, and the blue lines indicate the spacing

between the keyholes along the build direction). (c) Schematic illustration of the scanning speed variations during the single scanning trace and the corresponding melt pool shape; (d) scanning traces (red lines) of chess-scanned samples (the blue circle marks the single scanning trace, while the green circles indicate the overlap points between the neighbouring island); (e) schematic illustration of the definition of IS parameters and LBD settings; (f) the relationship between the samples' relative density fabricated using 4 J/mm^2 with different IS and LBD settings (inset is the BSE micrograph of the Ti-12Mo alloy fabricated using low LBD and 0.06 IS settings).

Fig. 6. (a)–(c) are the XRD pattern, low magnification and high magnification BSE images of Ti-12Mo alloy fabricated using a low AED of 1.6 J/mm^2, respectively; (d)–(f) are the XRD pattern, low magnification and high magnification BSE images of Ti-12Mo alloy fabricated using a high AED of 4 J/mm^2, respectively.

Fig. 7. (a) Schematic of the Ti-12Mo FGC with two designed low energy input layers; (b) the merged BSE micrograph of the FGC and the corresponding EDX elemental maps of Ti (c) and Mo (d).

Fig. 8. The microstructure of the interdiffusion area: (a) an EBSD IPF map of β phase; (b) KAM map of the β Ti matrix; (c) the phase distributions map of α" and β; (d) and (e) are the EDX elemental maps of Ti and Mo, respectively; (f) EDX line profiles of Ti and Mo elements' concentration along the solid white lines in (d) and (e); (g)–(i) are the BSE micrographs of the regions selected in (c), respectively.

Fig. 9. The microstructure of the matrix of the Ti-12Mo alloy fabricated using a high AED of 4 J/mm^2 (HE layer in FGC). (a) SEM micrograph showing the selected site for FIB milling with the inset showing the morphology of FIB lamella; (b) the HAADF-STEM image; (c) the bright-field TEM image and corresponding SAED pattern; (d) and (e) are the dark field TEM image showing ω1 and ω2 phases, respectively.

Fig. 10. The microstructure of the matrix of the Ti-12Mo alloy fabricated using a low AED of

1.6 J/mm^2 (LE layer in FGC). (a) SEM micrograph showing the selected site for FIB milling with the inset showing the morphology of FIB lamella; (b) and (c) are the bright-field TEM image and corresponding SAED pattern, respectively; (d) and (e) are the bright-field TEM image and corresponding SAED pattern from another region; (f)–(h) are the HAADF-STEM image and corresponding EDX elemental maps of Ti (g) and Mo (h), respectively.

Fig. 11. The microhardness profile across the Ti-Mo FGCs along the build direction (The interval between adjacent hardness tests is 0.1 mm).

Fig. 12. (a) The engineering (solid lines) and true (dotted lines) stress-strain curves of the LE, HE and FGC samples; (b) the strain-hardening rates of LE, HE and FGC samples.

Fig. 13. Compressive behaviours of the micropillars in LE and HE layers of FGC. (a) The engineering stress-strain curves; (b, c, d) the SEM image of the micropillar of LE: (a) as-milled, (c and d) after compression; (e, f, g) the SEM image of the micropillar of HE:(e) as-milled, (f and g) after compression.

Fig. 14. (a) The BF TEM image shows the microstructure of the FIB thin film, lifted out from the HE area in FGC specimens, which aligned with the compressive direction. (b) The BF TEM image, magnified from (a), with the SAED pattern inserted. (c) The DF TEM image shows the distribution of ω phases.

Fig. 15. (a) The BF TEM image shows the microstructure of the FIB thin film, lifted out from the LE area in FGC specimens, which aligned with the compressive direction. (b) The BF TEM image, magnified from (a), with the SAED pattern inserted. (c) The HAADF STEM image shows high-density dislocations.

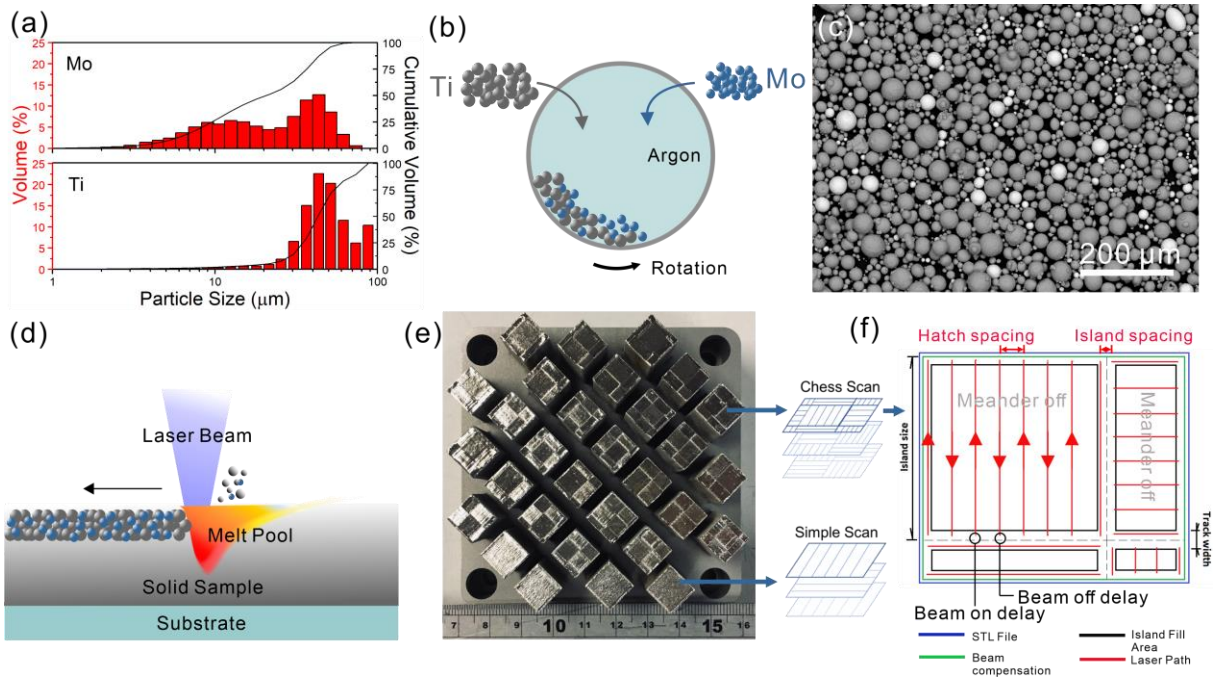

Fig. 1. (a) The particle size distributions of Ti and Mo elemental powders; (b) the schematic of the powder blending process; (c) BSE micrograph of Ti12Mo blended powder; (d) the schematic of LPBF in situ alloying processing; (e) as-fabricated samples with different scanning parameters; and (f) schematic illustration of the scanning strategies depicting the island spacing, and beam delay settings.

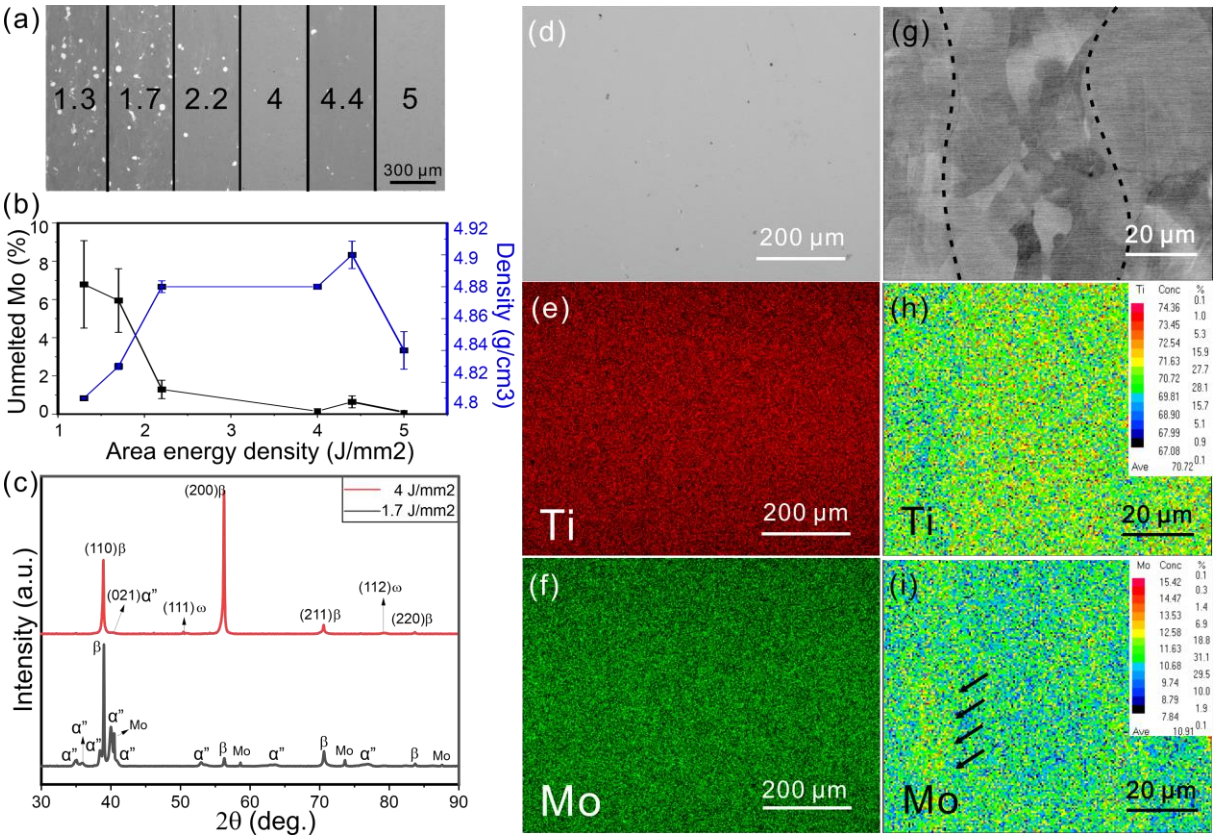

Fig. 2. (a) BSE images of as-fabricated Ti-12Mo specimens (values on the images are the AED); (b) effect of AED on the percentage of un-melted Mo and density; (c) XRD patterns of as-fabricated Ti-12Mo cube specimens; (d) BSE micrograph of Ti-12Mo sample; (e) and (f) are EDS elemental maps of Ti and Mo, respectively; (g) high magnification BSE micrograph (black dotted lines indicated the melt pool boundaries); (h) and (i) are the EPMA maps of Ti and Mo, respectively.

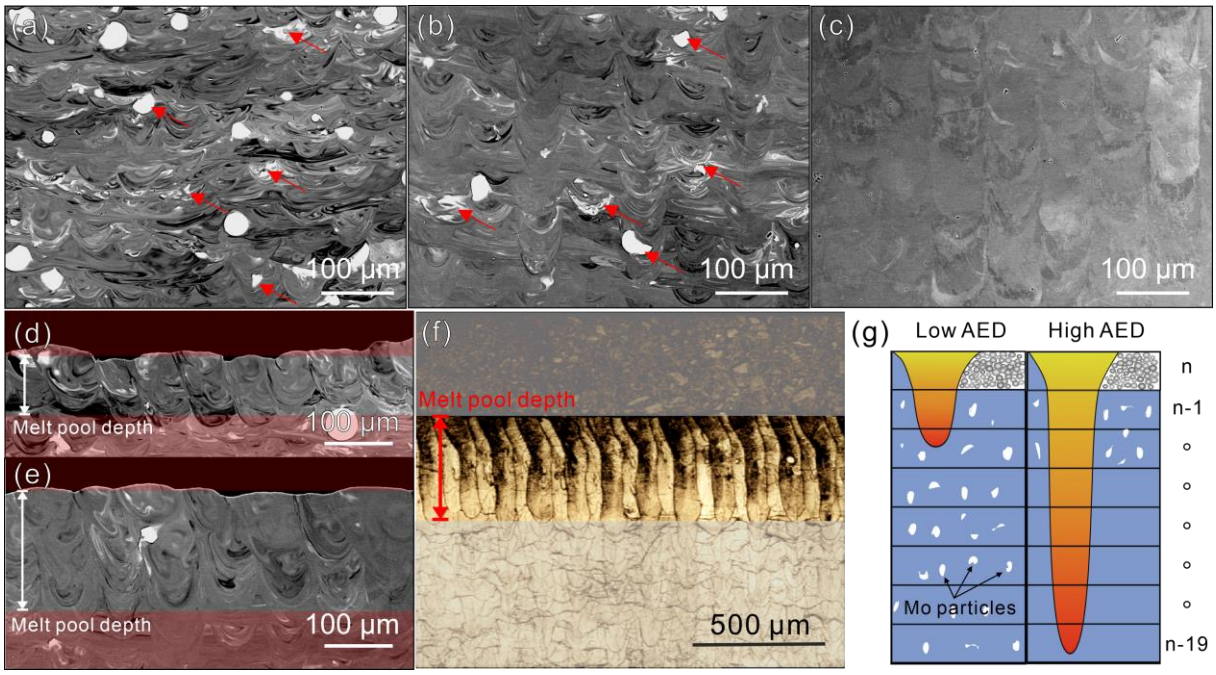

Fig. 3. (a)–(c) are BSE micrographs of the as-fabricated Ti-12Mo sample under different processing conditions: (a) low AED (1.7 J/mm^2), (b) middle AED (2.2 J/mm^2) and (c) high AED (4 J/mm^2); (d) and (e) are the side-view BSE images of the top layer of the samples fabricated using the AED of 1.7 and 2.2 J/mm^2, respectively; (f) the side-view optical micrograph of the top layer of the sample fabricated using AED of 4 J/mm^2; (g) the schematic illustration shows the remelting process of Mo particles during LPBF.

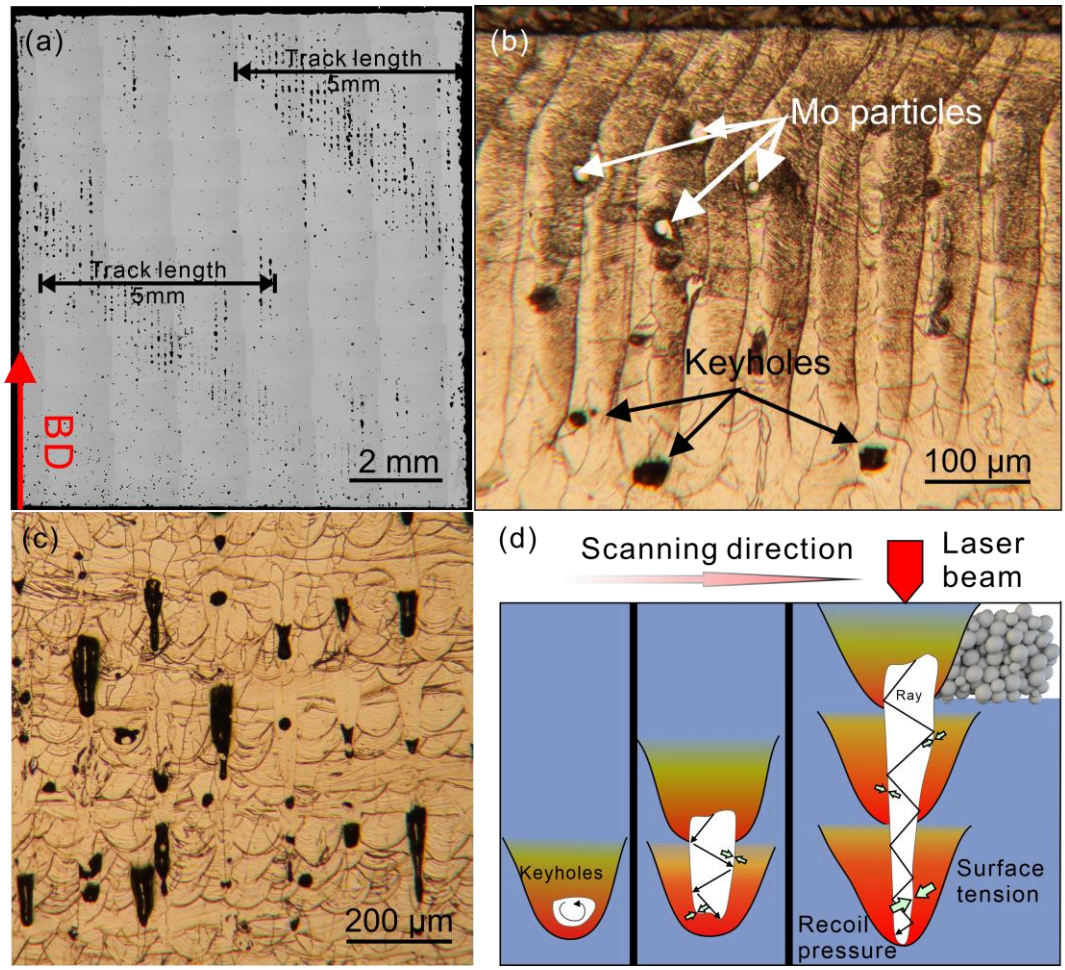

Fig. 4. (a) Optical micrograph of the full side section of the chess-scanned Ti-12Mo sample fabricated using AED of 4 J/mm^2, and high LBD settings; (b) and (c) are side-view optical micrographs of the keyholes of the chess-scanned Ti-12Mo alloy: (b) top layer; and (c) middle layer; and (d) the schematic illustration of the formation of keyholes defects.

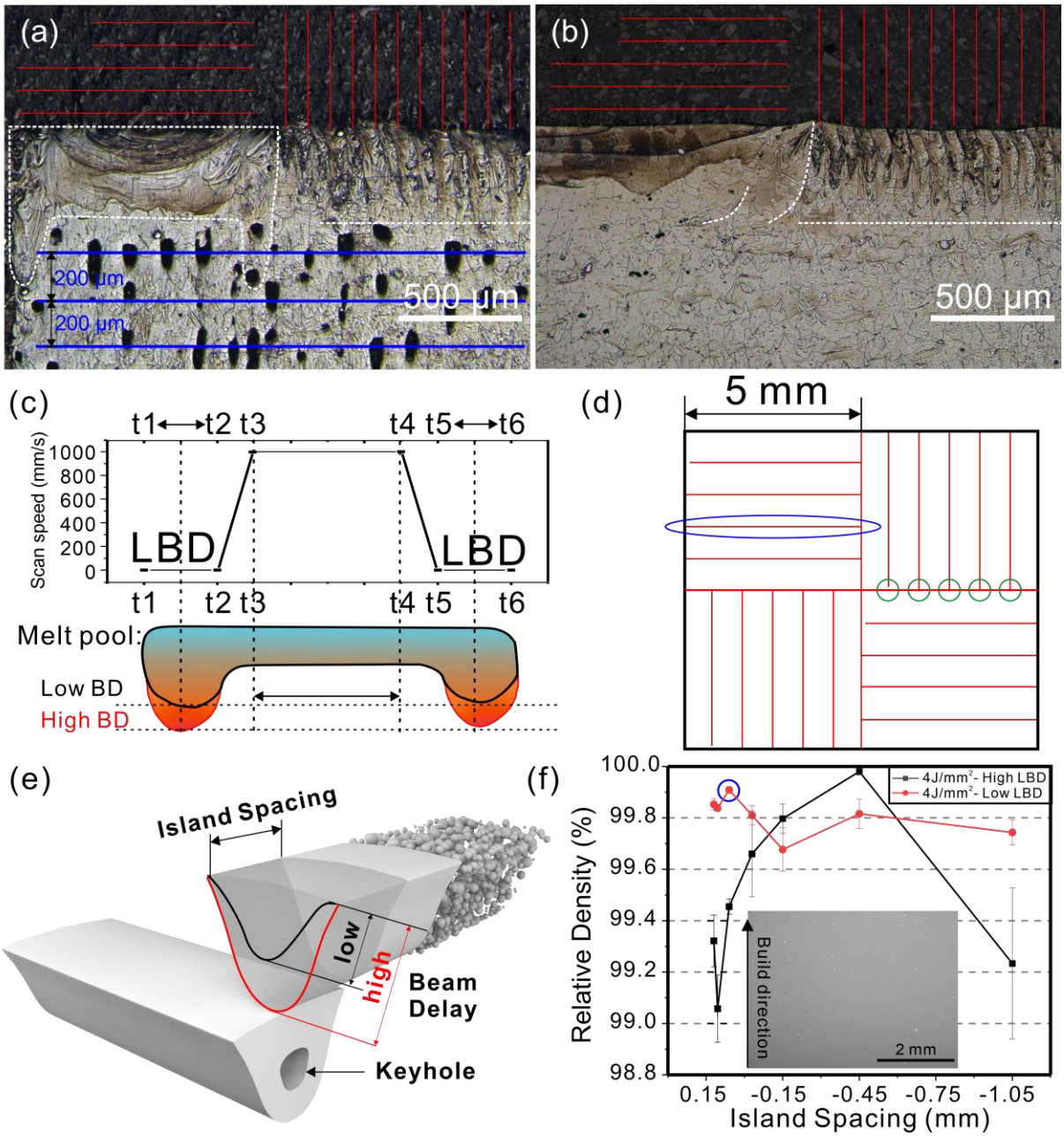

Fig. 5. The OM images of the specimens processed using chess scanning strategy with high LBD (a) and low LBD (b), respectively (Red lines indicate the scanning directions of the top layer, the white lines present some melt pool boundaries, and the blue lines indicate the spacing between the keyholes along the build direction). (c) Schematic illustration of the scanning speed variations during the single scanning trace and the corresponding melt pool shape; (d) scanning traces (red lines) of chess-scanned samples (the blue circle marks the single scanning trace, while the green circles indicate the overlap points between the neighbouring island); (e)

schematic illustration of the definition of IS parameters and LBD settings; (f) the relationship between the samples' relative density fabricated using 4 J/mm^2 with different IS and LBD settings (inset is the BSE micrograph of the Ti-12Mo alloy fabricated using low LBD and 0.06 IS settings).

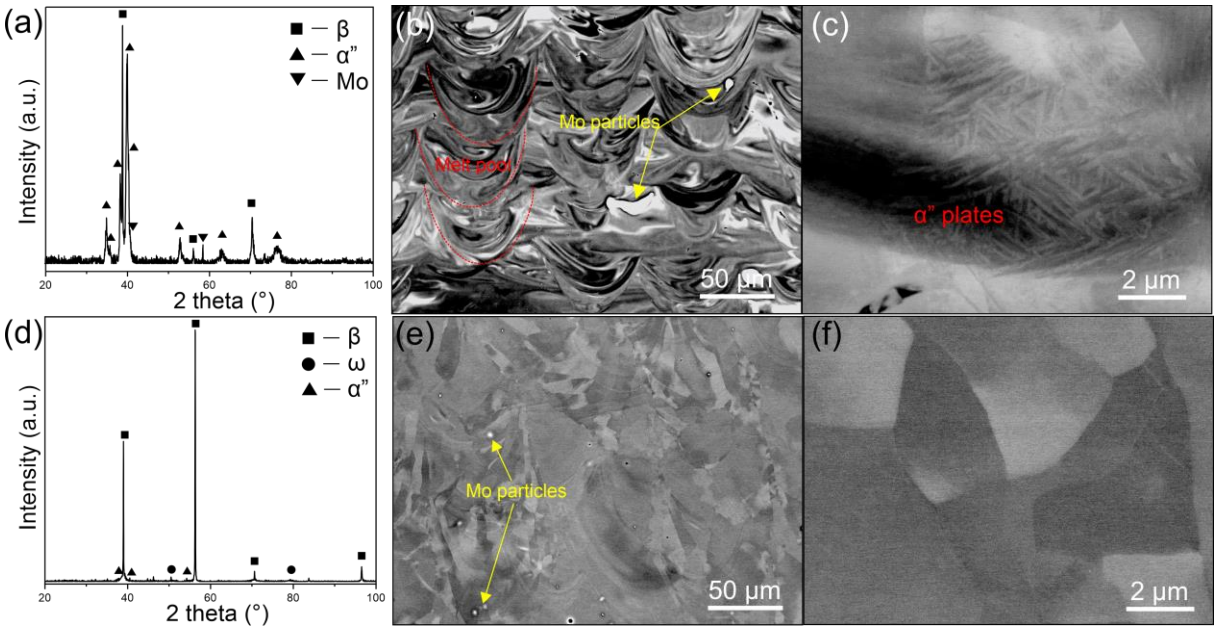

Fig. 6. (a)–(c) are the XRD pattern, low magnification and high magnification BSE images of Ti-12Mo alloy fabricated using a low AED of 1.6 J/mm^2, respectively; (d)–(f) are the XRD pattern, low magnification and high magnification BSE images of Ti-12Mo alloy fabricated using a high AED of 4 J/mm^2, respectively.

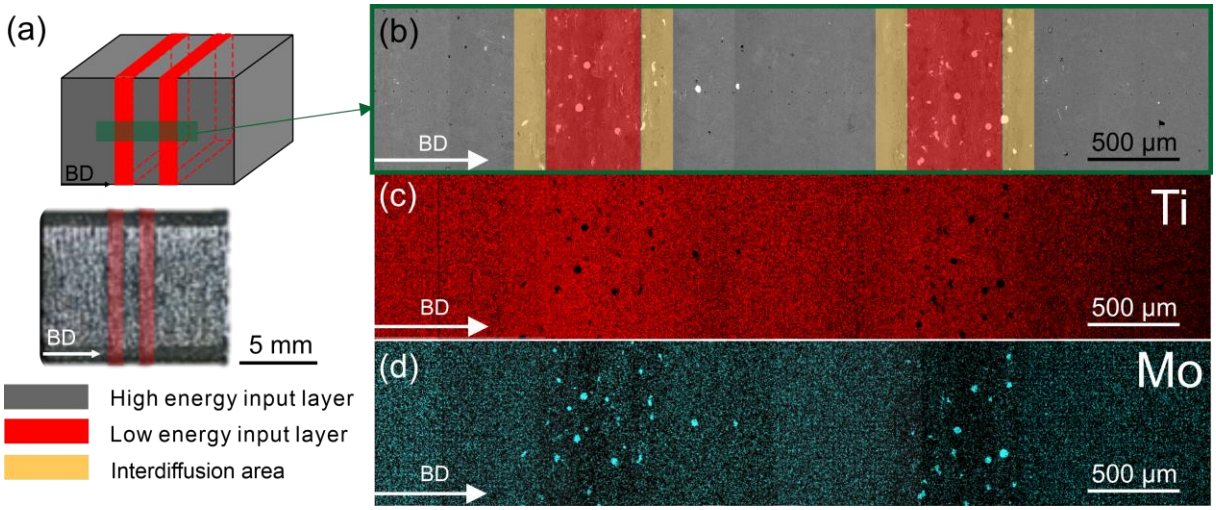

Fig. 7. (a) Schematic of the Ti-12Mo FGC with two designed low energy input layers; (b) the merged BSE micrograph of the FGC and the corresponding EDX elemental maps of Ti (c) and Mo (d).

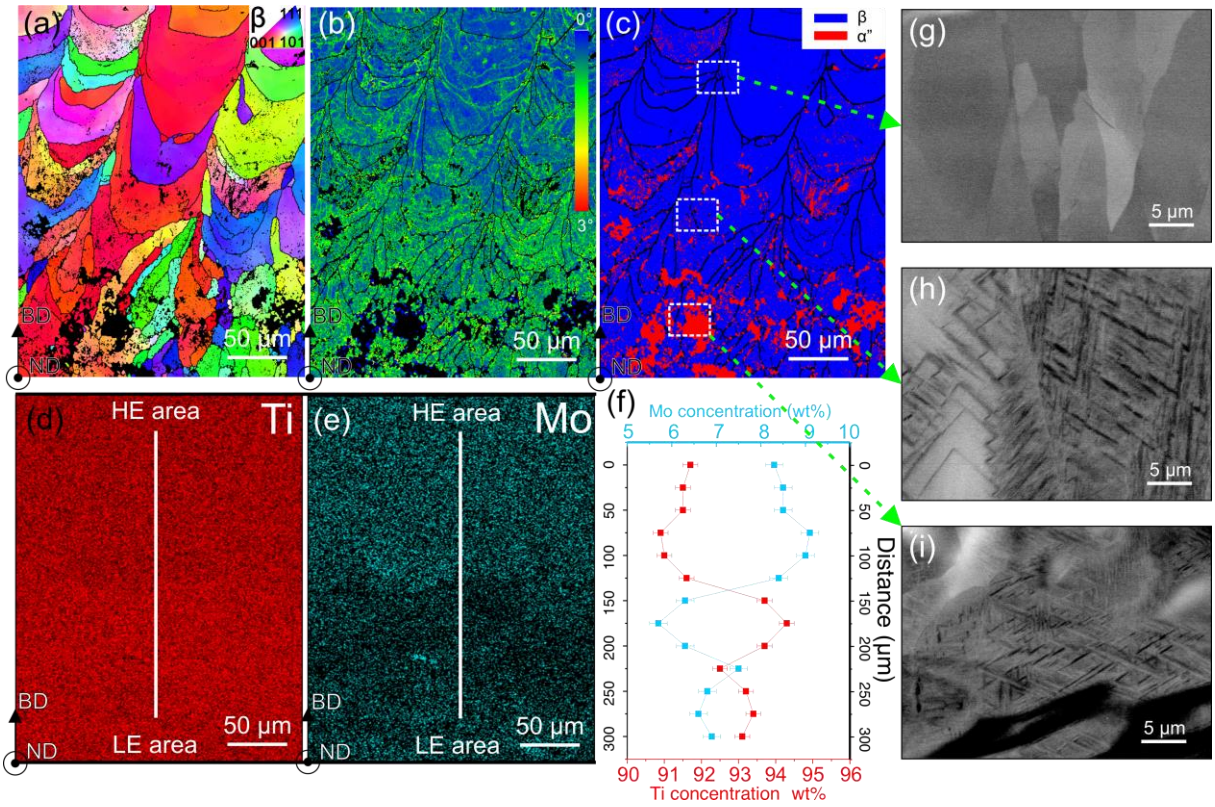

Fig. 8. The microstructure of the interdiffusion area: (a) an EBSD IPF map of β phase; (b) KAM map of the β Ti matrix; (c) the phase distributions map of α" and β; (d) and (e) are the EDX elemental maps of Ti and Mo, respectively; (f) EDX line profiles of Ti and Mo elements' concentration along the solid white lines in (d) and (e); (g)–(i) are the BSE micrographs of the regions selected in (c), respectively.

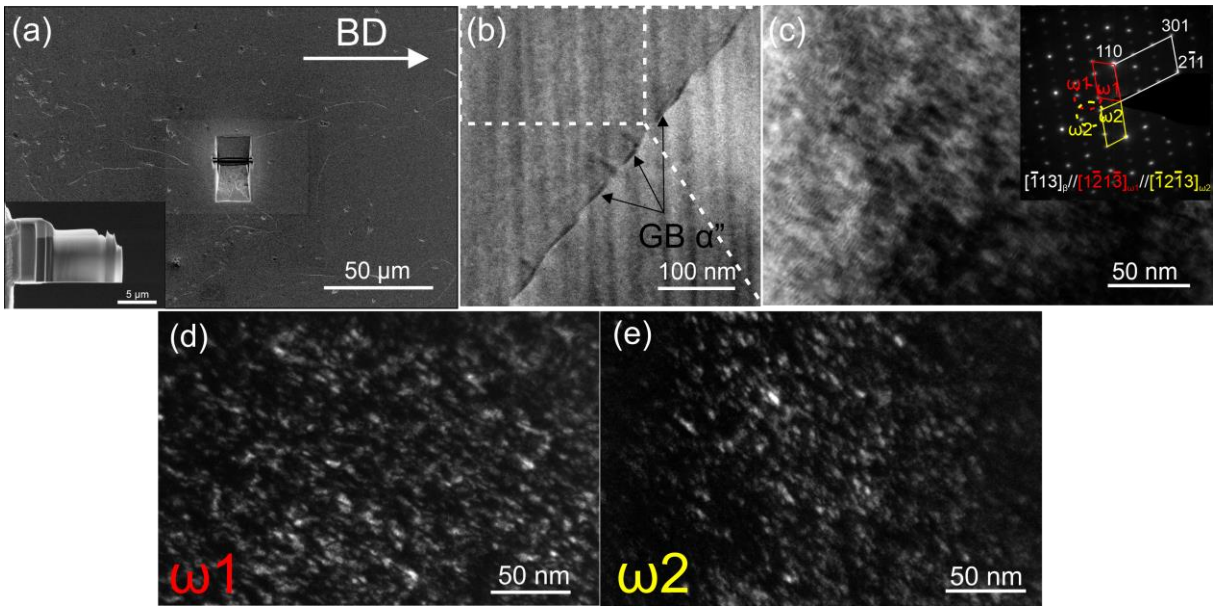

Fig. 9. The microstructure of the matrix of the Ti-12Mo alloy fabricated using a high AED of 4 J/mm^2 (HE layer in FGC). (a) SEM micrograph showing the selected site for FIB milling with the inset showing the morphology of FIB lamella; (b) the HAADF-STEM image; (c) the bright-field TEM image and corresponding SAED pattern; (d) and (e) are the dark field TEM image showing ω1 and ω2 phases, respectively.

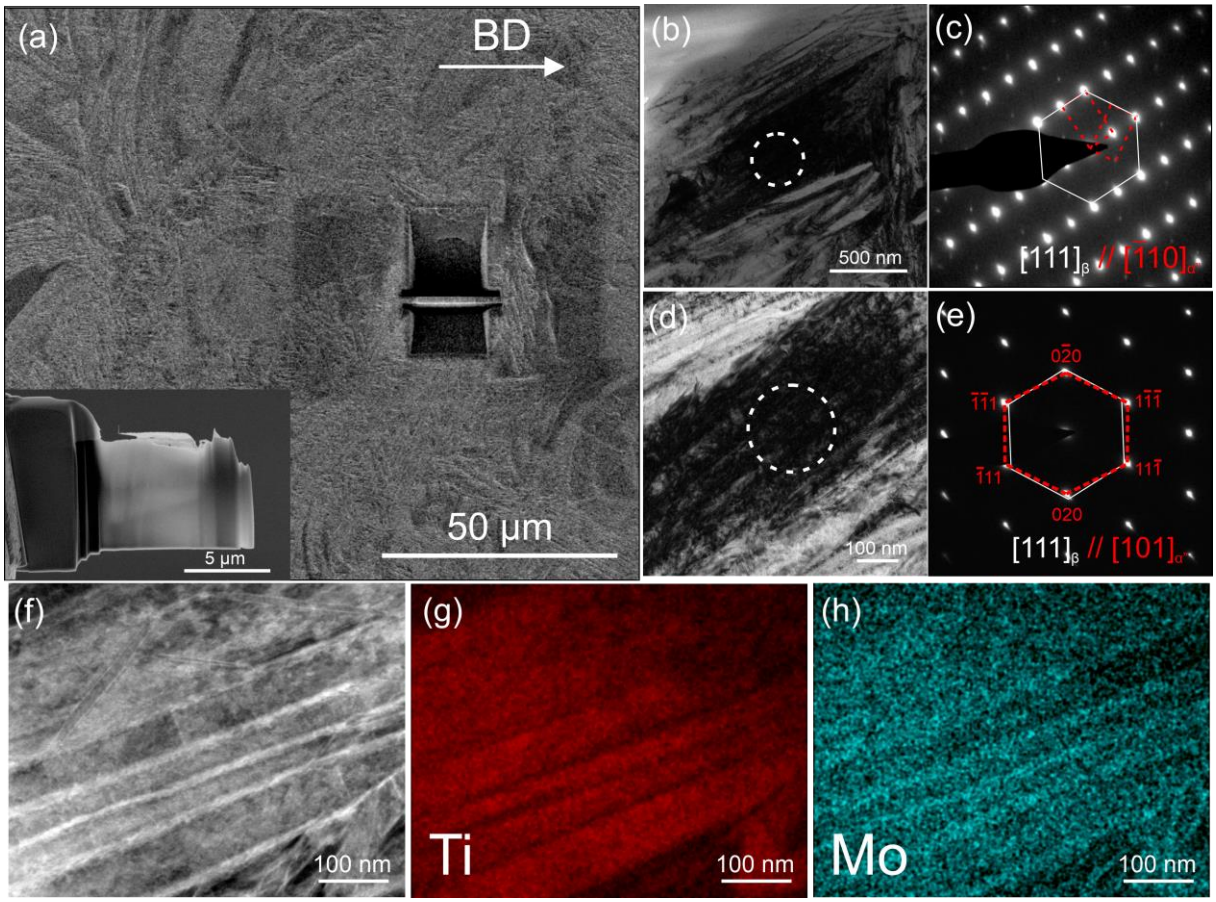

Fig. 10. The microstructure of the matrix of the Ti-12Mo alloy fabricated using a low AED of 1.6 J/mm^2 (LE layer in FGC). (a) SEM micrograph showing the selected site for FIB milling with the inset showing the morphology of FIB lamella; (b) and (c) are the bright-field TEM image and corresponding SAED pattern, respectively; (d) and (e) are the bright-field TEM image and corresponding SAED pattern from another region; (f)–(h) are the HAADF-STEM image and corresponding EDX elemental maps of Ti (g) and Mo (h), respectively.

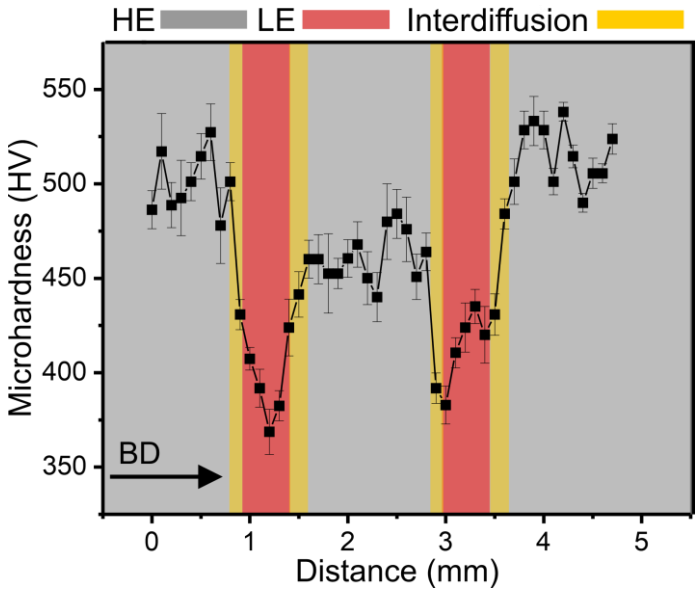

Fig. 11. The microhardness profile across the Ti-Mo FGCs along the build direction (The interval between adjacent hardness tests is 0.1 mm).

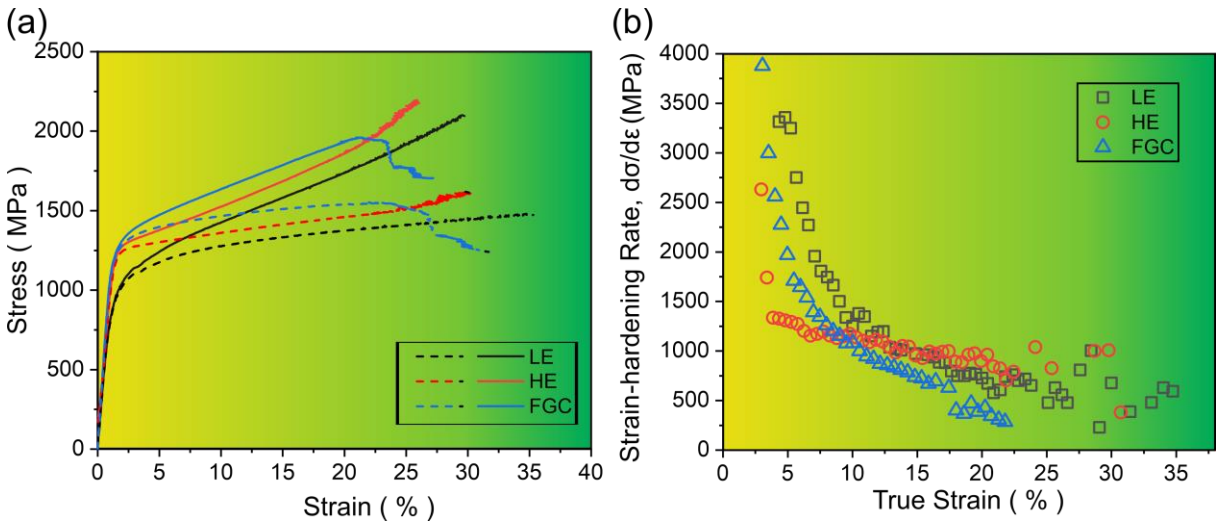

Fig. 12. (a) The engineering (solid lines) and true (dotted lines) stress-strain curves of the LE, HE and FGC samples; (b) the strain-hardening rates of LE, HE and FGC samples.

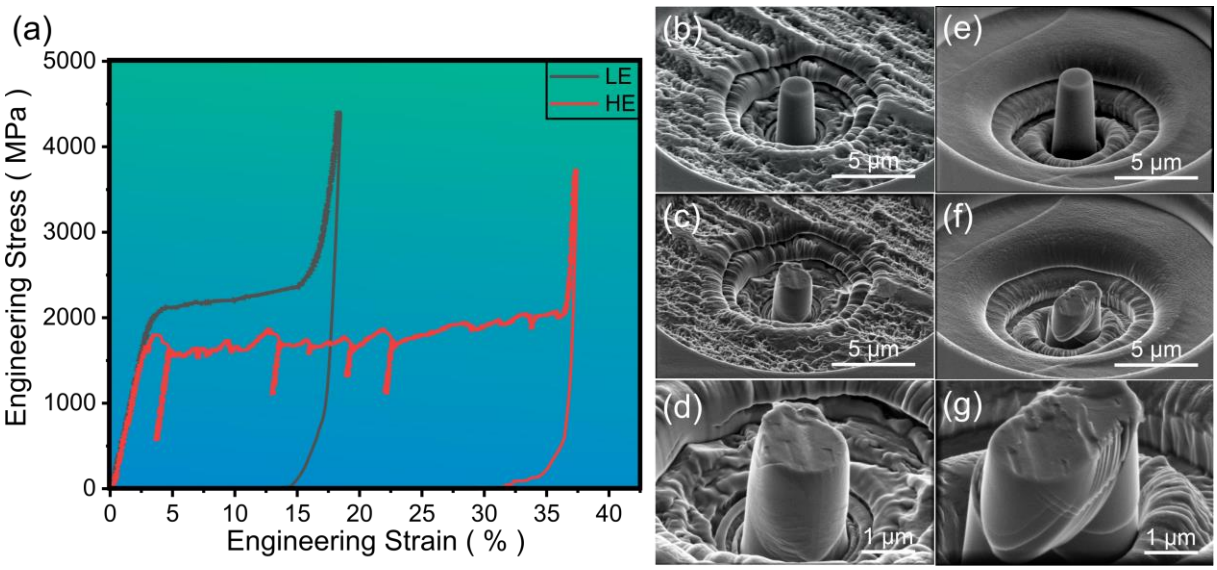

Fig. 13. Compressive behaviours of the micropillars in LE and HE layers of FGC. (a) The engineering stress-strain curves; (b, c, d) the SEM image of the micropillar of LE: (a) as-milled, (c and d) after compression; (e, f, g) the SEM image of the micropillar of HE:(e) as-milled, (f and g) after compression.

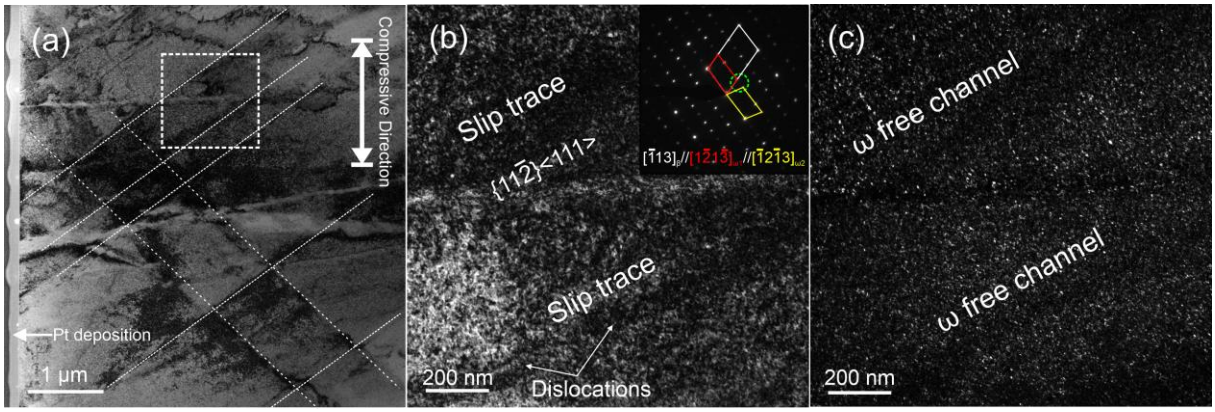

Fig.14. (a) The BF TEM image shows the microstructure of the FIB thin film, lifted out from the HE area in FGC specimens, which aligned with the compressive direction. (b) The BF TEM image, magnified from (a), with the SAED pattern inserted. (c) The DF TEM image shows the distribution of ω phases.

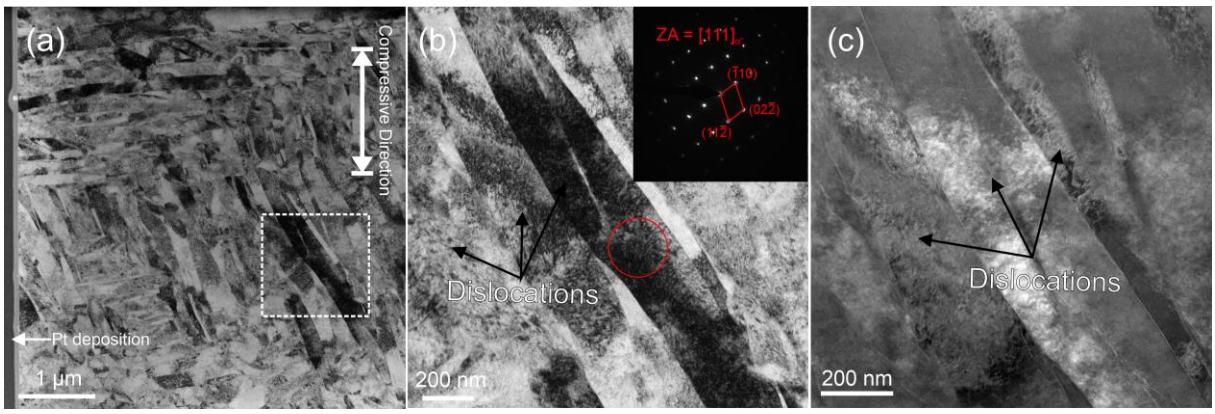

Fig.15. (a) The BF TEM image shows the microstructure of the FIB thin film, lifted out from the LE area in FGC specimens, which aligned with the compressive direction. (b) The BF TEM image, magnified from (a), with the SAED pattern inserted. (c) The HAADF STEM image shows high-density dislocations.